MÖSSBAUER EFFECT IN THULIUM 169

Thesis by

Richard Lewis Cohen

In Partial Fulfillment of the Requirements

For the Degree of

Doctor of Philosophy

California Institute of Technology

Pasadena, California

1962

Acknowledgments

Many people have contributed to the progress of these experiments. In particular, the author would like to thank:

Dr. Rudolf Mössbauer, who originally suggested the experiments reported on and who has since continually advanced the theoretical and experimental investigations. I would like to thank him particularly for much invaluable counsel and for instilling in the author an increased awareness of the need for precision in experimental work.

Drs. Ulrich Hauser and Felix Boehm, for many stimulating discussions and suggestions in the early stages of the experiment.

Herbert E. Henrikson, whose ingenuity and skill in the design of experimental equipment has enormously aided the progress of the investigations.

John M. Poindexter and Frank T. Snively, for invaluable help with the experimental work.

Vernon Stevens, Molly E. Cohen, Richard T. Brockmeier, J. David Bowman and Marshall Greer, for help with the measurements and data analysis.

Dr. Sten Samson, for much helpful information on the chemistry of thulium and erbium.

This research was supported in part by the Atomic Energy Commission.

Abstract

Mössbauer Effect in Tm^{169}

The recoil-free resonance absorption phenomenon has been used to study the 8.4 kev gamma ray which is emitted in the decay of the first excited state of Tm^{169} which is populated by the beta decay of Er^{169}. With sources and absorbers in various chemical forms, hyperfine structures which are strongly temperature dependent have been obtained. These have been studied with the aim of producing a source emitting an unsplit line. The observed absorption patterns are explained on the basis of a quadrupole interaction resulting from the interaction of the nuclear quadrupole moment of the excited state of Tm^{169} with the electric field gradient produced by the surrounding electrons and the crystal field. Arguments are given to show that the magnetic hyperfine interaction is expected to be negligible.

Table of Contents

I. Introduction

The discovery by R. L. Mössbauer (1) of the phenomenon of recoil-free gamma ray resonance emission and absorption has made possible various studies in nuclear and solid state physics and experimental tests of the theories of relativity. Most of these experiments have been performed using the isotope Fe^{57}, while relatively little has been done using other transitions, particularly those in the rare earth nuclei.

The unfilled 4f shell in the rare earths is the source of some physical properties which distinguish the rare earth series from most other elements. Mössbauer scattering experiments are particularly useful in studying the nuclear hyperfine splitting resulting from the interaction of the nuclear moments with internal fields produced by the atomic electrons.

There are several transitions in nuclei of rare earth atoms that can be used for recoil-free resonance absorption experiments (2, 3, 4). In the present work, the 8.4 kev gamma transition in Tm^{169} was selected. This particular transition, the characteristics of which are presented in fig. 1, has the advantages that the recoil-free fraction is large even at very high temperatures (see fig. 2) because of the low energy of the transition, that the half life of the level is long enough to give a narrow line width, and that suitable sources can easily be made by neutron irradiation of Er^{168}.

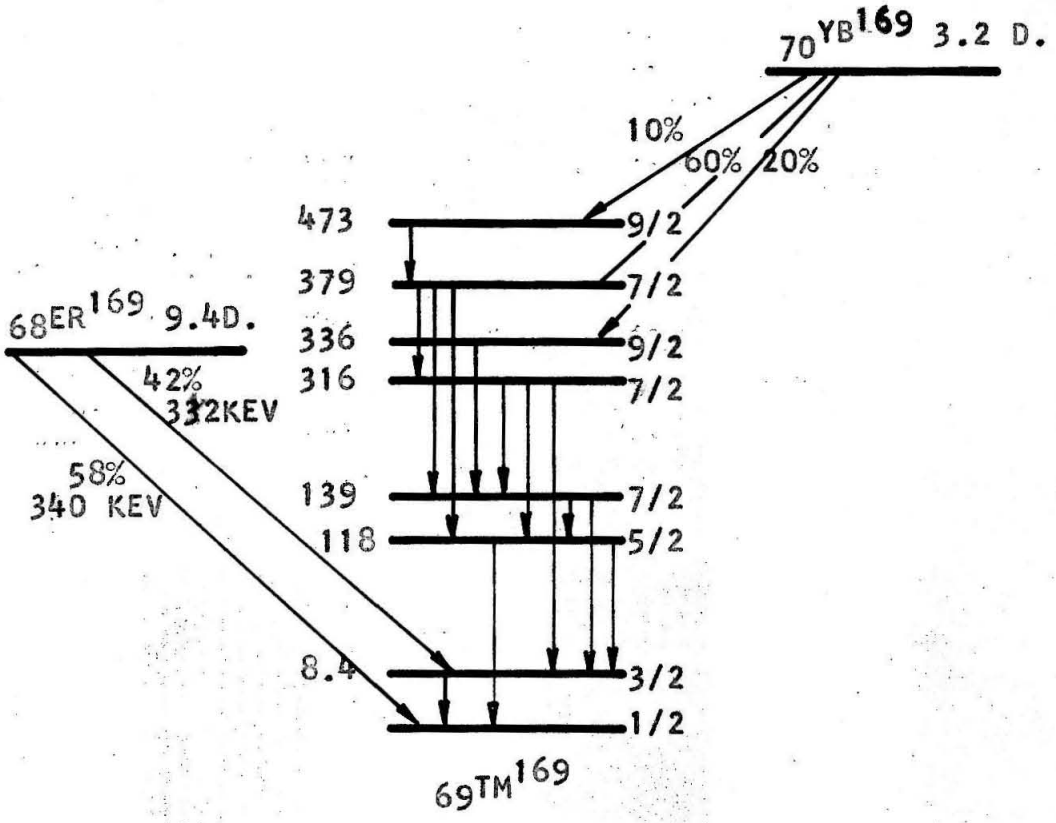

FIGURE 1: DECAY SCHEME OF THULIUM 169 SHOWING 8.4 KEV TRANSITION STUDIED IN PRESENT EXPERIMENTS

ADDITIONAL INFORMATION:
NATURAL THULIUM IS 100% THULIUM^{169}

GROUND STATE NUCLEAR MOMENT: -0.21 NM

8.4 KEV TRANSITION IS M1+ E2
INTERNAL CONVERSION COEFFICIENT M SHELL 69
N,O SHELL 37
8.4 KEV STATE HALF LIFE: 6.9×10^{-9}S.

FIGURE 2:
RECOIL-FREE FRACTION AS A FUNCTION OF TEMPERATURE FOR THE 8.4 KEV TRANSITION IN THULIUM^{169}

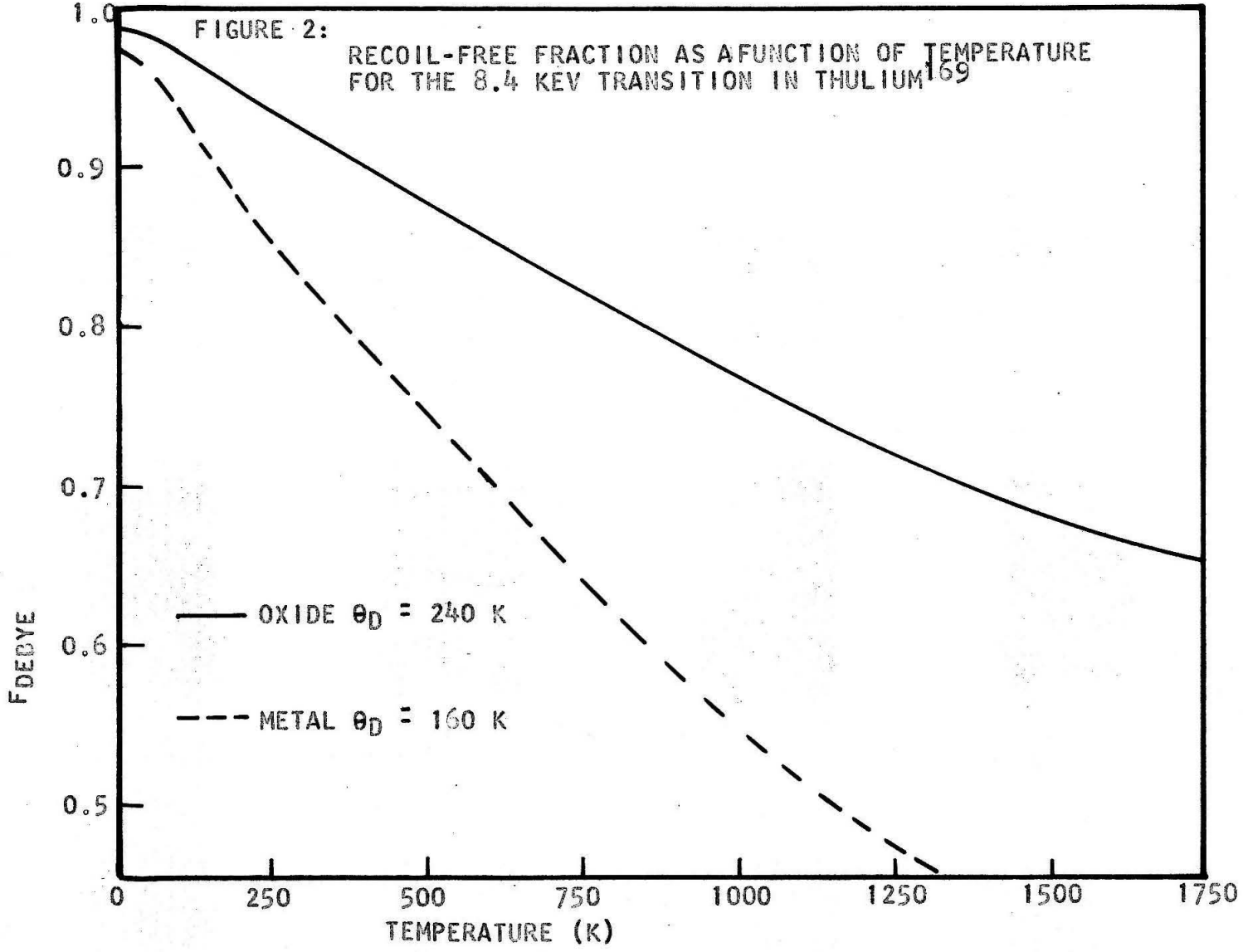

II. Theory

A. Elementary Theory of the Mössbauer Effect

The basis of all recoil-free* gamma-ray resonance experiments is the discovery by Mössbauer that when an atom is bound in a crystal its nucleus can make transitions in which the full energy of the transition is given to the emitted gamma ray and practically no recoil energy is given to the emitting or absorbing system. There are two basic parts to the analysis of the effect -- the part due to nuclear physics, which shows the origin and form of the resonance, and the part due to solid state physics, which shows how the recoil-free transitions occur.

The cross section for gamma-ray resonance absorption is given by the Breit-Wigner formula,

$$\sigma(E) = \frac{(2I_e+1)\hbar^2 c^2 \Gamma^2}{8\pi (2I_g+1)(1+\alpha_T)[(E-E_o)^2 + \Gamma^2/4]E^2} \quad (1)$$

where E_o is the difference between the ground- and excited-state energies, E is the energy of the incident gamma ray in the system of the absorbing nucleus, $\Gamma = \frac{\hbar}{\tau}$ is the total width of the level being excited, whose mean life is τ, I_e and I_g are the excited and ground state spins, and α_T is the total internal conversion coefficient for the transition.

---

* The name is somewhat misleading. It should be noted that it is not the recoil which is eliminated, but the energy loss due to recoil.

If only recoil-free transitions are being considered, this cross-section must be multiplied by the recoil-free fraction $f \leq 1$. Approximating the real vibration spectrum of the crystal by the Debye spectrum, we obtain for the recoil-free fraction (1)

$$F_{DEBYE} = \exp\left(-\frac{6R}{k\theta}\left[\frac{1}{4} + \left(\frac{T}{\theta}\right)^2 \int_0^{\theta/T} \frac{t\,dt}{e^t - 1}\right]\right) \quad (2)$$

where $R = E_o^2/2Mc^2$ is the recoil energy for a freely recoiling atom of mass M, and k is the Boltzmann constant. This formula gives the recoil-free fraction for emission or absorption of gamma rays from a nucleus in a crystal with Debye temperature θ, when the crystal is at temperature T.

B. Hyperfine Structure and Energy Shifts in Nuclear Transitions

In general, there are various effects which split and shift the line emitted from a Mössbauer source. In the present experiments, the large natural line width of the transition being studied prevents the observation of two of the possible effects. These are the second order Doppler shift due to thermal vibrations of the atom about its equilibrium lattice position (5) and an isomeric shift (6) which is an electric interaction due to the interaction of the nuclear charge distribution with the electron charge distribution inside the nuclear core, which can be made different for source and absorber.

The effects which are significant in the present study are the interaction between the nuclear quadrupole moment and the electric field gradient at the nucleus, and the magnetic dipole interaction between the nuclear magnetic moment and the magnetic field at the nuclear sites produced by the atomic electrons. These two effects are considered separately in the following sections.

The interaction of the nucleus with macroscopic externally applied fields is not large enough to be observable with the presently available field strengths.

1. The Quadrupole Interaction

The quadrupole interaction energy is a result of the interaction of the nuclear quadrupole moment with the electric field gradient at the nucleus. The interaction Hamiltonian can be written in the form $H_Q = \sum_{j=-2}^{j=2} Q_2^j \cdot (\nabla \vec{E})_2^{-j}$ (2), where Q_2^j is the nuclear quadrupole tensor with components

$$Q_2^0 = \frac{eQ}{2I(2I-1)} (3I_z^2 - I(I+1))$$

$$Q_2^{\pm 1} = \frac{eQ\sqrt{6}}{4I(2I-1)} (I_z I_\pm + I_\pm I_z) \qquad (3)$$

$$Q_2^{\pm 2} = \frac{eQ\sqrt{6}}{4I(2I-1)} I_\pm^2$$

where $I_\pm$ and I_z are to be treated as operators on the nuclear spin wave function $|I,m\rangle$ which has spin I and spin projection m_I along an arbitrarily chosen z axis. $I_\pm$ and I_z are defined by

$$I_\pm |I,m\rangle = (I_x \pm i I_y)|I,m\rangle = [(I \mp m)(I \pm m + 1)]^{1/2} |I, m \pm 1\rangle$$

$$I_z |I,m\rangle = m|I,m\rangle.$$

$(\nabla \vec{E})_2^j$ is a form of the electric field gradient tensor with components

$$(\nabla \vec{E})_2^0 = \frac{1}{2} U_{zz}$$

$$(\nabla \vec{E})_2^{\pm 1} = \frac{1}{\sqrt{6}} (U_{xz} \pm i U_{yz}) \qquad (4)$$

$$(\nabla \vec{E})_2^{\pm 2} = \frac{1}{2\sqrt{6}} (U_{xx} - U_{yy} \pm 2i U_{xy})$$

with U the potential at the nuclear site and $U_{x_\mu x_\nu} = \frac{\partial^2}{\partial x_\mu \partial x_\nu} U$.

We are completely free in the choice of coordinate axes. Without the application of external fields, the system that is most convenient for calculation is that in which the principal axes of the gradient tensor serve as the coordinate axes in which to write the nuclear wave function. In this system, which we will call the (x', y', z') system, the gradient components $U_{x'y'} = U_{y'z'} = U_{x'z'} = 0$. In addition, we will conform to the convention of having the z' axis along the strongest component of the gradient tensor. We further introduce the parameters $\eta = (U_{y'y'} - U_{x'x'}) / U_{z'z'}$ and $eq = U_{z'z'}$. η and eq then completely describe the gradient tensor in the (x', y', z') system when Laplace's equation holds.

We will now proceed to calculate the quadrupole splitting of the Tm^{169} nuclear energy levels in the (x', y', z') system. Since the ground state has $I = \frac{1}{2}$, there will be no quadrupole splitting. The matrix elements for the quadrupole perturbation of the I = 3/2 excited state (8.4 kev) can be calculated using equations 3 and 4:

$$\langle I,m|H_Q|I,m\rangle = \langle I,m|\sum_{-2}^{2} Q_2^j\cdot(\nabla\vec{E})_2^{-j}|I,m\rangle = A\left(3m^2 - I(I+1)\right)$$

$$\langle I,m|H_Q|I\,m'\rangle = \langle I,m|\sum Q_2^j\cdot(\nabla\vec{E})_2^{-j}|I,m'\rangle = \frac{\eta A}{2}\langle I_+^2 + I_-^2\rangle$$

$$A = \frac{qe^2Q}{4I(2I-1)}$$

The resulting perturbation matrix is

$m \downarrow$ / $m' \rightarrow$	$3/2$	$1/2$	$-1/2$	$-3/2$
$3/2$	$3A$	0	$\sqrt{3}\eta A$	0
$1/2$	0	$-3A$	0	$\sqrt{3}\eta A$
$-1/2$	$\sqrt{3}\eta A$	0	$-3A$	0
$-3/2$	0	$\sqrt{3}\eta A$	0	$3A$

An exact solution of the secular equation of this matrix yields the energy eigenvalues

$$E_{\pm 3/2} = 3A\,(1+\eta^2/3)^{1/2} \qquad (5a)$$

$$E_{\pm 1/2} = -3A\,(1+\eta^2/3)^{1/2} \qquad (5b)$$

the eigenfunctions of which are

$$|I,\pm 3/2\rangle' = A_{\pm 3/2}\,|I,\pm 3/2\rangle + B_{\pm 1/2}\,|I,\pm \tfrac{1}{2}\rangle \quad \text{AND} \qquad (6a)$$

$$|I,\pm 1/2\rangle' = C_{\pm 1/2}\,|I,\pm 1/2\rangle + D_{\pm 3/2}\,|I,\pm 3/2\rangle \qquad (6b)$$

(the wave functions are identified by the I_z value they assume for $\eta \rightarrow 0$)

Thus without performing the actual diagonalization of the gradient tensor, we have shown that under a pure quadrupole interaction the $I = 3/2$ excited state is split into two levels regardless of the complexity of the gradient tensor.

The field gradient at the nuclear sites comes from the surrounding ions and from distortions of the electronic shells produced by the field of these ions. The first step in evaluating the field gradient, therefore, will be to look at the structure of the crystal and the electronic states of the rare earth ions in the crystal electric field.

2. Crystal Fields and Perturbations of the 4f Electronic Shell in Rare Earth Ions

The rare earth series of elements is distinguished by the fact that the 4f electronic shell is partially filled. The electronic configuration for all these elements can be written (7) $1s^2 2s^2 2p^6 3s^2 3p^6 3d^{10} 4s^2 4p^6 4d^{10} 4f^n 5s^2 5p^6 5d^{0-1} 6s^2$. In compounds or solutions, three electrons go off (the two 6s electrons, the 5d electron, if any, and a 4f electron if there is no 5d electron), leaving a 3+ ion with a partially filled 4f shell shielded by the surrounding closed shells of 5s and 5p electrons. The magnetic properties of the 3+ ion are determined essentially by the 4f electrons, since all the other electrons are in closed shells.

The free ion can usually be described accurately using L-S coupling of the 4f electrons; this gives a free ion ground state with $\vec{J} = \vec{L} + \vec{S}$ which is $2J + 1$ fold degenerate. If we place the ion in the electric field generated by the surrounding ions in a crystal, we find that the shielding of the 4f electrons by a total of eight 5s and 5p electrons makes the effect of the crystal field weak in comparison with the L-S coupling, so that J remains a good quantum number and perturbation methods can be used to evaluate the electron configuration of the ion in the crystal electric field. This is in marked contrast to the iron transition elements, where the perturbing effect of the crystal field is strong in comparison with the L-S coupling and J is no longer a good quantum number.

The effect of the crystal field is to partly or completely remove the degeneracy of the free ion ground state, depending on the

crystal field symmetry.* The crystal field splits the energy levels of the free ion ground state by less than 0.1 ev ($\sim 1200^{\circ}$ K) for Tm^{3+}(8), while the spacing between levels of different J is of the order of a few ev ($\sim 30,000^{\circ}$ K) (8). Therefore, in calculating the effect of the crystal field perturbation on the free ion ground state, in first order the existence of excited states can be neglected.

Because of the weak coupling ($\sim 10^{-5}$ ev) between the electronic states and nuclear moments, the hyperfine interaction can be neglected in calculating the electronic wave functions.

We shall proceed to calculate the form of the 4f electronic wave functions resulting from the perturbation of the free ion energy levels by the crystal field.

Since in first order the crystal electric field splits the ground state of the free ion into a manifold of electronic states of the same J, it is convenient to expand the potential in terms of spherical harmonics,

$$V(\vec{r}) = \sum_{n,\nu} A_{n\nu} Y_n^{\nu} r^n \qquad (7)$$

This expansion holds inside a volume that has no free charge, and is restricted to relatively few terms because of the symmetry of the crystal field. Table I contains the only values of the expansion parameters n and ν which occur in equation 7 for some of the compounds studied in the present experiment.

---

* In Tm^{3+}, which has an even number of electrons, there is no Kramers degeneracy.

Table I

Significant Constants in the Expansion of the Crystal Field for Various Lattice Symmetries

Hexagonal close packed structure:
Point symmetry D_{3h}

n	ν
2	0
3	±3
4	0
5	± 3
6	0, ± 6

Body-centered cubic structure:
Point symmetry C_2

n	ν
1	0
2	0, ± 2
3	0, ± 2
4	0, ± 2, ± 4
5	0, ± 2, ± 4
6	0, ± 2, ± 4, ± 6

Body-centered cubic structure:
Point symmetry C_{3i}

n	ν
2	0
4	0, ± 3
6	0, ± 3, ± 6

The matrix elements of the potential operator of equation 7 taken in the manifold of eigenstates having the same J are given by

$$V_{m\,m'} = \langle \Psi_{J,m} \mid V(\vec{r}) \mid \Psi_{J,m'} \rangle = \langle \Psi_{J,m} \mid \sum_{n,\nu} A_{n\nu}\, Y_n^{\nu}\, r^n \mid \Psi_{J,m'} \rangle \quad (8)$$

The wave functions

$$\Psi_i = \sum_m \alpha_{im}\, \Psi_{J,m} \quad (9)$$

for the different crystal symmetries follow from the solutions of the secular determinant of equation 8. Results for the ground state of Tm^{3+} are presented in Table II.

As can be seen from equations 8 and 9, the actual numerical values of the coefficients α_{im} in Table II depend on the values of $A_{n\nu}$ which characterize the crystal field and on the expectation values of r^n.

We are concerned here only with some basic characteristics of the hyperfine interaction, which can be obtained without a numerical evaluation of the α_{im}. This numerical evaluation is difficult in most cases because values for $A_{n\nu}$ are generally not known.

Table IIa

Secular Determinant and Wave Functions for the Ground State of Tm^{3+} (Configuration $3H_6$)

Point Symmetry D_{3h}

Secular Determinant

m' ►	6	0	-6	3	-3	4	-2	-4	2	5	-1	-5	1
m ▼ 6	V_{66}	V_{60}	V_{6-6}										
0	V_{06}	V_{00}	V_{0-6}										
-6	V_{-66}	V_{-60}	V_{-6-6}										
3				V_{33}	V_{3-3}								
-3				V_{-33}	V_{-3-3}								
4						V_{44}	V_{4-2}						
-2						V_{-24}	V_{-2-2}						
-4								V_{-4-4}	V_{-42}				
2								V_{2-4}	V_{22}				
5										V_{55}	V_{5-1}		
-1										V_{-15}	V_{-1-1}		
-5												V_{-5-5}	V_{-51}
1												V_{1-5}	V_{11}

Table IIa (cont'd)

Wave Functions

Level Number (Arbitrary)	Degeneracy	Wave Functions
1	1	$\alpha_{16}(Y_6^6 + Y_6^{-6}) + \alpha_{10}Y_6^0$
2	1	$\alpha_{26}(Y_6^6 + Y_6^{-6}) + \alpha_{20}Y_2^0$
3	1	$\alpha_{36}(Y_6^6 + Y_6^{-6}) + \alpha_{30}Y_6^0$
4	1	$(Y_6^3 + Y_6^{-3}) / \sqrt{2}$
5	1	$(Y_6^3 - Y_6^{-3}) / \sqrt{2}$
6	2	$\alpha_{64}Y_6^4 + \alpha_{6-2}Y_6^{-2}$
		$\alpha_{6-4}Y_6^{-4} + \alpha_{62}Y_6^2$
7	2	$\alpha_{74}Y_6^4 + \alpha_{7-2}Y_6^{-2}$
		$\alpha_{7-4}Y_6^{-4} + \alpha_{72}Y_6^2$
8	2	$\alpha_{85}Y_6^5 + \alpha_{8-1}Y_6^{-1}$
		$\alpha_{8-5}Y_6^{-5} + \alpha_{81}Y_6^1$
9	2	$\alpha_{95}Y_6^5 + \alpha_{9-1}Y_6^{-1}$
		$\alpha_{9-5}Y_6^{-5} + \alpha_{91}Y_6^1$

Table IIb

Secular Determinant and Wave Functions for the Ground State of Tm^{3+} (Configuration $^3H_6$)

Point Symmetry C_2

Secular Determinant

m' ►	6	4	2	0	-2	-4	-6	5	3	1	-1	-3	-5
m ▼ 6	V_{66}	V_{64}	V_{62}	V_{60}	0	0	0						
4	V_{46}	V_{44}	V_{42}	V_{40}	V_{4-2}	0	0						
2	V_{26}	V_{24}	V_{22}	V_{20}	V_{2-2}	V_{2-4}	0						
0	V_{06}	V_{04}	V_{02}	V_{00}	V_{0-2}	V_{0-4}	V_{0-6}						
-2	0	V_{-24}	V_{-22}	V_{-20}	V_{-2-2}	V_{-2-4}	V_{-2-6}						
-4	0	0	V_{-42}	V_{-40}	V_{-4-2}	V_{-4-4}	V_{-4-6}						
-6	0	0	0	V_{-60}	V_{-6-2}	V_{-6-4}	V_{-6-6}						
5								V_{55}	V_{53}	V_{51}	V_{5-1}	0	0
3								V_{35}	V_{33}	V_{31}	V_{3-1}	V_{3-3}	0
1								V_{15}	V_{13}	V_{11}	V_{1-1}	V_{1-3}	V_{1-5}
-1								V_{-15}	V_{-13}	V_{-11}	V_{-1-1}	V_{-1-3}	V_{-1-5}
-3								0	V_{-33}	V_{-31}	V_{-3-1}	V_{-3-3}	V_{-3-5}
-5								0	0	V_{-51}	V_{-5-1}	V_{-5-3}	V_{-5-5}

Table IIb (cont'd)

Wave Functions

Level Number (Arbitrary)	Degeneracy	Wave Functions
1	-	$\alpha_{16}Y_6^6 + \alpha_{14}Y_6^4 + \alpha_{12}Y_6^2 + \alpha_{10}Y_6^0 + \alpha_{1-2}Y_6^{-2} + \alpha_{1-4}Y_6^{-4} + \alpha_{1-6}Y_6^{-6}$
2	-	$\alpha_{26}Y_6^6 + \alpha_{24}Y_6^4 + \alpha_{22}Y_6^2 + \alpha_{20}Y_6^0 + \alpha_{2-2}Y_6^{-2} + \alpha_{2-4}Y_6^{-4} + \alpha_{2-6}Y_6^{-6}$
3	-	$\alpha_{36}Y_6^6 + \alpha_{34}Y_6^4 + \alpha_{32}Y_6^2 + \alpha_{30}Y_6^0 + \alpha_{3-2}Y_6^{-2} + \alpha_{3-4}Y_6^{-4} + \alpha_{3-6}Y_6^{-6}$
4	-	$\alpha_{46}Y_6^6 + \alpha_{44}Y_6^4 + \alpha_{42}Y_6^2 + \alpha_{40}Y_6^0 + \alpha_{4-2}Y_6^{-2} + \alpha_{4-4}Y_6^{-4} + \alpha_{4-6}Y_6^{-6}$
5	-	$\alpha_{56}Y_6^6 + \alpha_{54}Y_6^4 + \alpha_{52}Y_6^2 + \alpha_{50}Y_6^0 + \alpha_{5-2}Y_6^{-2} + \alpha_{5-4}Y_6^{-4} + \alpha_{5-6}Y_6^{-6}$
6	-	$\alpha_{66}Y_6^6 + \alpha_{64}Y_6^4 + \alpha_{62}Y_6^2 + \alpha_{60}Y_6^0 + \alpha_{6-2}Y_6^{-2} + \alpha_{6-4}Y_6^{-4} + \alpha_{6-6}Y_6^{-6}$
7	-	$\alpha_{76}Y_6^6 + \alpha_{74}Y_6^4 + \alpha_{72}Y_6^2 + \alpha_{70}Y_6^0 + \alpha_{7-2}Y_6^{-2} + \alpha_{7-4}Y_6^{-4} + \alpha_{7-6}Y_6^{-6}$
8	-	$\alpha_{85}Y_6^5 + \alpha_{83}Y_6^3 + \alpha_{81}Y_6^1 + \alpha_{8-1}Y_6^{-1} + \alpha_{8-3}Y_6^{-3} + \alpha_{8-5}Y_6^{-5}$
9	-	$\alpha_{95}Y_6^5 + \alpha_{93}Y_6^3 + \alpha_{91}Y_6^1 + \alpha_{9-1}Y_6^{-1} + \alpha_{9-3}Y_6^{-3} + \alpha_{9-5}Y_6^{-5}$
10	-	$\alpha_{105}Y_6^5 + \alpha_{103}Y_6^3 + \alpha_{101}Y_6^1 + \alpha_{10-1}Y_6^{-1} + \alpha_{10-3}Y_6^{-3} + \alpha_{10-5}Y_6^{-5}$
11	-	$\alpha_{115}Y_6^5 + \alpha_{113}Y_6^3 + \alpha_{111}Y_6^1 + \alpha_{11-1}Y_6^{-1} + \alpha_{11-3}Y_6^{-3} + \alpha_{11-5}Y_6^{-5}$
12	-	$\alpha_{125}Y_6^5 + \alpha_{123}Y_6^3 + \alpha_{121}Y_6^1 + \alpha_{12-1}Y_6^{-1} + \alpha_{12-3}Y_6^{-3} + \alpha_{12-5}Y_6^{-5}$
13	-	$\alpha_{135}Y_6^5 + \alpha_{133}Y_6^3 + \alpha_{131}Y_6^1 + \alpha_{13-1}Y_6^{-1} + \alpha_{13-3}Y_6^{-3} + \alpha_{13-5}Y_6^{-5}$

Table IIc

Secular Determinant and Wave Functions for the Ground State of Tm^{3+} (Configuration $^3H_6$)

Point Symmetry C_{3i}

Secular Determinant

m' ►	6	3	0	-3	-6	5	2	-1	-4	-5	-2	1	4
m 6	V_{66}	V_{63}	V_{60}	0	0								
▼ 3	V_{36}	V_{33}	V_{30}	V_{3-3}	0								
0	V_{06}	V_{03}	V_{00}	V_{0-3}	V_{0-6}								
-3	0	V_{-33}	V_{-30}	V_{-3-3}	V_{-3-6}								
-6	0	0	V_{-60}	V_{-6-3}	V_{-6-6}								
5						V_{55}	V_{52}	V_{5-1}	0				
2						V_{25}	V_{22}	V_{2-1}	V_{2-4}				
-1						V_{-15}	V_{-12}	V_{-1-1}	V_{-1-4}				
-4						0	V_{-42}	V_{-4-1}	V_{-4-4}				
-5										V_{-5-5}	V_{-5-2}	V_{-5+1}	0
-2										V_{-2-5}	V_{-2-2}	V_{-21}	V_{-24}
1										V_{1-5}	V_{1-2}	V_{11}	V_{14}
4										0	V_{4-2}	V_{41}	V_{44}

Table IIc (cont'd)

Wave Functions

Level Number (Arbitrary)	Degeneracy	Wave Functions
1	-	$\alpha_{16}Y_6^6 + \alpha_{13}Y_6^3 + \alpha_{10}Y_6^0 + \alpha_{1-3}Y_6^{-3} + \alpha_{1-6}Y_6^{-6}$
2	-	$\alpha_{26}Y_6^6 + \alpha_{23}Y_6^3 + \alpha_{20}Y_6^0 + \alpha_{2-3}Y_6^{-3} + \alpha_{2-6}Y_6^{-6}$
3	-	$\alpha_{36}Y_6^6 + \alpha_{33}Y_6^3 + \alpha_{30}Y_6^0 + \alpha_{3-3}Y_6^{-3} + \alpha_{3-6}Y_6^{-6}$
4	-	$\alpha_{46}Y_6^6 + \alpha_{43}Y_6^3 + \alpha_{40}Y_6^0 + \alpha_{4-3}Y_6^{-3} + \alpha_{4-6}Y_6^{-6}$
5	-	$\alpha_{56}Y_6^6 + \alpha_{53}Y_6^3 + \alpha_{50}Y_6^0 + \alpha_{5-3}Y_6^{-3} + \alpha_{5-6}Y_6^{-6}$
6	2	$\alpha_{65}Y_6^5 + \alpha_{62}Y_6^2 + \alpha_{6-1}Y_6^{-1} + \alpha_{6-4}Y_6^{-4}$ $\alpha_{6-5}Y_6^{-5} + \alpha_{6-2}Y_6^{-2} + \alpha_{61}Y_6^1 + \alpha_{64}Y_6^4$
7	2	$\alpha_{75}Y_6^5 + \alpha_{72}Y_6^2 + \alpha_{7-1}Y_6^{-1} + \alpha_{7-4}Y_6^{-4}$ $\alpha_{7-5}Y_6^{-5} + \alpha_{7-2}Y_6^{-2} + \alpha_{71}Y_6^1 + \alpha_{74}Y_6^4$
8	2	$\alpha_{85}Y_6^5 + \alpha_{82}Y_6^2 + \alpha_{8-1}Y_6^{-1} + \alpha_{8-4}Y_6^{-4}$ $\alpha_{8-5}Y_6^{-5} + \alpha_{8-2}Y_6^{-2} + \alpha_{81}Y_6^1 + \alpha_{84}Y_6^4$
9	2	$\alpha_{95}Y_6^5 + \alpha_{92}Y_6^2 + \alpha_{9-1}Y_6^{-1} + \alpha_{9-4}Y_6^{-4}$ $\alpha_{9-5}Y_6^{-5} + \alpha_{9-2}Y_6^{-2} + \alpha_{91}Y_6^1 + \alpha_{94}Y_6^4$

3. Influence of Relaxation Phenomena

In principle, each of the different electronic states Ψ_i produces a different electric field gradient, which we will call $(\nabla \vec{E})_i$, and a different magnetic field, $\vec{H}_i$, and therefore a different hyperfine splitting. This would lead to a large number of nuclear levels in the nuclear excited and ground states, which would produce an exceedingly complicated gamma spectrum. However, the spin-lattice relaxation performs an averaging process which considerably simplifies the results.

When rare earth ions are bound in crystals, there is a strong interaction between the J of the $4f$ electrons and the lattice. Because the orbital angular momentum is not quenched, the electron spin-lattice relaxation times are very short (substantially less than 10^{-10} s (9) at room temperature), much shorter than in the case of the iron transition elements. This time is shorter than both the lifetime of the nuclear state ($\sim 10^{-8}$ s) and the nuclear precession period ($\sim 10^{-9}$ s). The nucleus does not follow the rapid reorientations of the electronic spins because of the weak coupling between $\vec{I}$ and $\vec{J}$, and therefore experiences average values of $\nabla\vec{E}$" and $\vec{H}$ resulting from an average over the electronic states. This means that we can restrict the averaging procedure to the electronic states only.

Assuming that the averaging process over the electronic states takes place in times very much smaller than the nuclear lifetime and the nuclear precession period, we obtain the following averages:

$$\overline{\nabla \vec{E}''} = \frac{\sum_i [\exp(-E_i/kT)]\, \nabla \vec{E}_i''}{\sum_i \exp(-E_i/kT)} \qquad (10)$$

$$\overline{\vec{H}} = \frac{\sum_i [\exp(-E_i/kT)]\, \vec{H}_i}{\sum_i \exp(-E_i/kT)} \qquad (11)$$

where $\exp(-E_i / kT)$ is the Boltzmann population factor for the electronic state with energy E_i and T is the lattice temperature. The averaging is shown schematically in fig. 3.

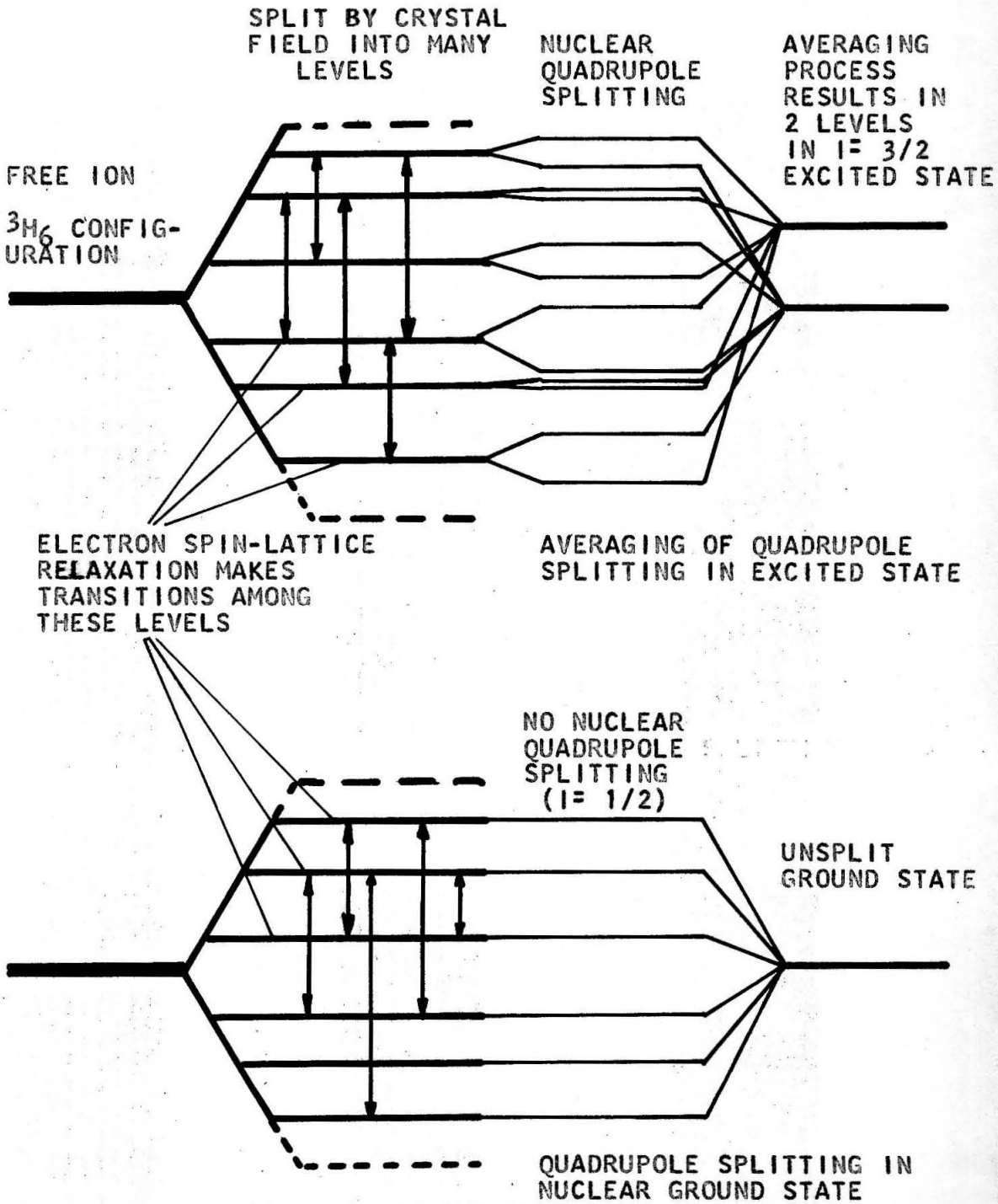

FIGURE 3: ILLUSTRATION OF THE AVERAGING OF THE QUADRUPOLE SPLITTING BY THE SPIN-LATTICE RELAXATION PROCESS.

4. The Effective Quadrupole Interaction

The electric field gradient at the nucleus of an ion in an ionic crystal results from four principal sources:

a. the direct field gradient $\nabla\vec{E}'$ due to the surrounding ions

b. the distortion of the filled electronic shells by the field of the surrounding ions

c. the distortion of partially filled shells by the field of the surrounding ions resulting in $\nabla\vec{E}''$

d. the distortion of the filled shells by the field resulting from the partially filled shells, resulting in $\nabla\vec{E}'''$.

These components will be analyzed in the above order.

a. In ions of the rare earth series, as will be shown, $\nabla\vec{E}'$ is relatively small and can be neglected.

b. The second effect is called "antishielding" since the net effect of the distortions of the closed shells is to increase the field gradient $\nabla\vec{E}'$ resulting from the direct crystal field. The antishielding effect can be considered in either of two complementary ways.

The first viewpoint assumes that the field due to the nuclear quadrupole moment deforms the electronic shells of the atom, inducing

a quadrupole moment in them which is $-\gamma$ times the nuclear quadrupole moment. The quadrupole moment of the atom is then $(1-\gamma)$ times the nuclear quadrupole moment (if the induced moment is in the same direction as the nuclear moment). If the atom is placed in a perturbing field gradient and the energy splitting between the nuclear orientations is measured, the direction of the induced quadrupole moment changes with the nuclear orientation, and the total quadrupole interaction is then given by

$$H_Q = (Q_{atom}) \cdot \nabla \vec{E}' = (1-\gamma) Q_{nuclear} \cdot \nabla \vec{E}'$$

where $\nabla \vec{E}'$ is the gradient tensor of the crystal field.

The second viewpoint is that if an atom is placed in an inhomogeneous electric field, this field will distort the filled electronic shells, and this distortion produces a gradient at the nucleus which augments or decreases the gradient from the externally applied field.

As has been shown by Sternheimer (10), these two viewpoints are equivalent in first order, i.e., as long as the deformation of the electronic shells is small, which is normally the case.

Using the first of these analyses, which is more generally useful and easier to deal with than the second, Sternheimer (10) has calculated the size of this effect for various closed shell ions. We can make an estimate of γ for the closed shells of the Tm^{3+} ion by starting with Sternheimer's value of $\gamma = -143 \pm 10\%$ for the Cs^+ ion, which has the same closed shells as the Tm^{3+} ion. The existing calculations reveal a rough variation of γ with $1/Z^2$ for a given shell. Therefore we assume a somewhat smaller value of γ for Tm^{3+} $(Z = 69)$

than for Cs^+ ($Z = 55$). We will use $\gamma = -100$ in further calculations. Since $|\gamma| \gg 1$, we can neglect $\nabla \vec{E}'$ in comparison with $\gamma \nabla \vec{E}'$.

c. The distortion of the partially filled 4f shell by the crystal field is the main source of the electric field gradient, and will be analyzed in some detail. As each of the different 4f electronic states produces a different field gradient at the nucleus, we shall separately calculate the field gradients $(\nabla \vec{E})''_i$ for each of the different electronic substates characterized by ψ_i, the general wave function obtained earlier for the 4f electrons.

We evaluate the gradient tensor $(\nabla \vec{E})''_i$ as follows: Assuming that all the 4f electronic charge is outside the spheroid of nuclear shape,

$$\phi(\vec{r}) = \int \frac{\rho(\vec{r}')d\vec{r}'}{|\vec{r} - \vec{r}'|} = 2e \int \frac{\psi^*(\vec{r}')\,\psi(\vec{r}')d\vec{r}'}{|\vec{r} - \vec{r}'|}$$

where $\phi(\vec{r})$ is the potential in the neighborhood of the nucleus from the 4f electrons and $\vec{r}'$ is the variable over which we integrate the electronic charge. Expanding $|\vec{r} - \vec{r}'|^{-1}$ in spherical harmonics and differentiating under the integral sign, we obtain the Cartesian components of $(\nabla \vec{E})''_i$:

$$\phi_{xx} = 2e\left\langle \sqrt{\frac{\pi}{15}}\left(Y_2^2 + Y_2^{-2}\right) - \frac{2}{3}\sqrt{\frac{\pi}{5}}\,Y_2^0 \right\rangle \langle r^{-3} \rangle$$

$$\phi_{yy} = 2e\left\langle -\sqrt{\frac{\pi}{15}}\left(Y_2^2 + Y_2^{-2}\right) - \frac{2}{3}\sqrt{\frac{\pi}{5}}\,Y_2^0 \right\rangle \langle r^{-3} \rangle$$

$$\phi_{zz} = 2e\left\langle \frac{4}{3}\sqrt{\frac{\pi}{5}}\,Y_2^0 \right\rangle \langle r^{-3} \rangle$$

$$\phi_{xy} = 2e\left\langle -i\sqrt{\frac{\pi}{15}}\left(Y_2^2 - Y_2^{-2}\right)\right\rangle \langle r^{-3}\rangle$$

$$\phi_{xz} = 2e\left\langle \sqrt{\frac{\pi}{15}}\left(Y_2^1 + Y_2^{-1}\right)\right\rangle \langle r^{-3}\rangle$$

$$\phi_{yz} = 2e\left\langle -i\sqrt{\frac{\pi}{15}}\left(Y_2^1 - Y_2^{-1}\right)\right\rangle \langle r^{-3}\rangle .$$

From this we obtain that in the case of the D_{3h} symmetry (see page 14) $\phi_{xy} = \phi_{yz} = \phi_{xz} = 0$. This means that the principal axes of the field gradient tensor lie along the coordinate system used to express the crystal field; this is not true for the C_2 and C_{3i} symmetries.

d. $(\nabla \vec{E})'''$, the part of the field gradient resulting from the distortion of the closed shells by the field of the 4f electrons, is very difficult to calculate precisely. In principle, it could be calculated by perturbing the closed shell wave functions with the potential due to the 4f electrons, but the extensive overlap of the 4f wave functions with the closed shell wave functions (which are themselves not well known for the rare earth series) makes the integrals very difficult. However, we can give some qualitative arguments to justify the assumption that $\nabla \vec{E}''' \ll \nabla \vec{E}''$, i.e., that the field gradient produced indirectly by the 4f electrons through the polarization of the closed shells is considerably smaller than the direct field gradient from the 4f electrons. It can be shown (11) that $\langle r^{-3}\rangle$ for the outer shells with $\ell \neq 0$* is considerably smaller

---

* S states are not perturbed in first order by the 4f electrons, and shall not be considered.

than $\langle r^{-3} \rangle$ for the 4f electrons. Since the gradient at the nuclear sites is proportional to the angular integrals $\langle Y_2^m \rangle$ (which are of the same order of magnitude for all the shells) and proportional to $\langle r^{-3} \rangle$, $\nabla \vec{E}'''$ is smaller than $\nabla \vec{E}''$ even under strong deformations of the filled shells and will be neglected hereafter.

Thus, it has been shown that the major contributions to the field gradient at the nucleus come from the assymetry of the 4f electron shell and the antishielding of the crystal field, so that

$$\nabla \vec{E} \doteq \nabla \vec{E}'' + \gamma \nabla \vec{E}' \quad . \tag{12}$$

As explained on page 17, when the spin-lattice relaxation time is short, we cannot observe the field gradients $(\nabla \vec{E})_i''$ for each electronic substate but rather observe an average field gradient $\overline{\nabla \vec{E}''}$ which results from the different electronic states weighted according to their Boltzmann factors (eq. 10). The total effective field gradient is then

$$\overline{\nabla \vec{E}} = \overline{\nabla \vec{E}''} + \gamma \nabla \vec{E}' \quad . \tag{13}$$

$\gamma \nabla \vec{E}'$ is not influenced by the averaging process.

$\gamma \nabla \vec{E}'$ is essentially independent of the temperature, so that any temperature variation of $\overline{\nabla \vec{E}}$ comes only from $\overline{\nabla \vec{E}''}$. The temperature dependence of the field gradient $\overline{\nabla \vec{E}}$ is then as follows: At very low temperatures ($kT << E_1$), only the lowest electronic state is populated, and $\overline{\nabla \vec{E}''}$ is $\nabla \vec{E}_1''$ for the lowest electronic state. At intermediate temperatures ($kT \approx E_1$), all the electronic states are populated and $\overline{\nabla \vec{E}''}$ is given by the average from equation 10. At high temperatures ($kT >> E_1$) all the electron substates will be equally

populated, which means that there will be no preferred orientation of $\vec{J}$. This results in a net charge distribution of spherical symmetry which produces a zero field gradient at the nucleus. The quadrupole interaction produced by the $4f$ electrons will therefore approach zero at high temperatures. However, by means of the antishielding effect, the $4f$ electrons still contribute a small field gradient which can be calculated by treating the $4f$ shell as a charge distribution of spherical symmetry, like the closed shells.

Thus, at high temperatures, the remaining effective field gradient is approximately $\gamma \nabla \vec{E}'$.

5. The Effective Magnetic Interaction

The magnetic hyperfine interaction is given by

$$H_m = \vec{\mu}_n \cdot \vec{H} \qquad (14)$$

where μ_n is the nuclear magnetic moment and $\vec{H}$ is the magnetic field at the nucleus. In the absence of an external magnetic field, the field at the nucleus results from the spin and orbital angular momenta of the atomic electrons in partially filled shells, in our case the 4f shells.

Under the assumption of pure L-S coupling, equation 14 can be rewritten (11)

$$H_m = K\vec{I} \cdot \vec{J} = K(I_xJ_x + I_yJ_y + I_zJ_z) \qquad (15)$$

where the constant K contains such things as radial integrals, electronic charge, and g-factors.

If the coupling between $\vec{I}$ and $\vec{J}$ is assumed negligible (see page 17), the only significant term in equation 15 is KI_zJ_z, so that

$$\langle H_m \rangle = K \langle I_z \rangle \langle J_z \rangle \quad . \qquad (16)$$

As in the case of the quadrupole interaction, we first evaluate $\langle H_m \rangle$ for each of the different electronic states. It is necessary to treat the degenerate and non-degenerate states separately.

For the non-degenerate electronic levels, we can show that the magnetic interaction is zero in each state. The non-degenerate electronic wave functions are real except for a trivial phase factor because the crystal field Hamiltonian (eq. 7), which does not contain magnetic interactions, is invariant under time reversal. Thus the electronic wave functions contain equal admixtures of Y_J^m and Y_J^{-m} .

$\langle J_z \rangle = 0$ for states of this form; thus the magnetic hyperfine interaction vanishes for the non-degenerate electronic levels.

If the electronic states are degenerate, the situation is more complex. If we consider a doubly degenerate state with wave functions ψ_A and ψ_B, the general wave functions for the degenerate level are given by

$$\psi_1 = a_1 \psi_A + b_1 \psi_B \qquad |a_1|^2 + |b_1|^2 = 1$$

$$\psi_2 = a_2 \psi_A + b_2 \psi_B \qquad |a_2|^2 + |b_2|^2 = 1$$
$$a_1^* a_2 + b_1^* b_2 = 0 .$$

At higher temperatures, we must consider the fact that the electron spin-lattice relaxation is so fast that all the electronic states are populated during the time of the nuclear decay and so we must average over the population. Since ψ_1 and ψ_2 are degenerate, the Boltzmann factor will be the same for each, and the average magnetic field at the nucleus from this degenerate level is

$$\tfrac{1}{2}\langle \psi_1 | J_z | \psi_1 \rangle + \tfrac{1}{2}\langle \psi_2 | J_z | \psi_2 \rangle =$$
$$= \tfrac{1}{2}\left[|a_1|^2 \langle \psi_A | J_z | \psi_A \rangle + |b_1|^2 \langle \psi_B | J_z | \psi_B \rangle + |a_2|^2 \langle \psi_A | J_z | \psi_A \rangle + |b_2|^2 \langle \psi_B | J_z | \psi_B \rangle \right]$$
$$= \tfrac{1}{2}\left[(|a_1|^2 + |a_2|^2) \langle \psi_A | J_z | \psi_A \rangle + (|b_1|^2 + |b_2|^2) \langle \psi_B | J_z | \psi_B \rangle \right]$$
$$= \tfrac{1}{2}\left[\langle \psi_A | J_z | \psi_A \rangle + \langle \psi_B | J_z | \psi_B \rangle \right] .$$

Since the submatrices of the crystal field perturbation (see Table II) from which ψ_A and ψ_B were found are Hermitian conjugates,

if $\psi_A = \sum_m \alpha_m Y_J^m$

then $\psi_B = \sum_{-m} \beta_{-m} Y_J^{-m}$ with $|\beta_{-m}| = |\alpha_m|$.

(no Y_J^k appears in both ψ_A and ψ_B)

Then

$$\langle \psi_A | J_z | \psi_A \rangle = \sum_m |\alpha_m|^2 m$$

$$\langle \psi_B | J_z | \psi_B \rangle = \sum_{-m} |\beta_{-m}|^2 (-m)$$

so that

$$\langle \psi_A | J_z | \psi_A \rangle + \langle \psi_B | J_z | \psi_B \rangle = 0,$$

and thus no doublet state gives any hyperfine interaction if the electronic spin-lattice relaxation time is short compared to $\sim 10^{-10}$ seconds.

Since only the degenerate states contribute to the magnetic interaction, the averaging by the spin-lattice relaxation process is less critical with respect to the relaxation time than that of the quadrupole interaction.

6. The Nuclear Quadrupole Moment of Tm^{169}

Nuclei in the range A = 150 - 190 are normally well described by the unified model of Bohr, Mottelson, and Nilsson (12, 13). In this model, an odd A nucleus is considered as a core containing all the nucleons but the last (odd) nucleon, which then moves in the field of the core. The core is deformed into an axially symmetric ellipsoid. Nuclear states can be made from combinations of rotational states of the core and intrinsic states of the last nucleon, with the angular momenta of the core and the odd particle combining to give I, the net nuclear spin.

The predictions of the above model (see 13) are in good agreement with the spectrum of Tm^{169} studied experimentally by Boehm et al (14). The $I = \frac{1}{2}$ ground state of Tm^{169} is the lowest state of a 1/2, 3/2, 5/2, 7/2, 9/2 rotational band, and the 8.4 kev (I = 3/2) excited state studied in the present experiment corresponds to the second state of that band. Some excited states corresponding to intrinsic excitations of the odd proton are also observed in the decay scheme of Tm^{169} (fig. 1).

The unified model allows us to make estimates of the nuclear moments. We can calculate the quadrupole moment for the 8.4 kev state by assuming that the single particle contribution will be small in comparison to that from the deformed core. Then the Nilsson model (13) gives

$$Q = \left[\frac{3K^2 - I(I+1)}{(I+1)(2I+3)}\right] \cdot \frac{4}{5} \delta Z R_0^2 (1 + \delta/2 + \cdots)$$

where $K = \frac{1}{2}$ is the projection of I on the axis of symmetry of the core, δ is the deformation of the core, and Z and R_o are the charge and the mean radius of the nucleus. Using (13) $\delta = 0.28$ and $R_o = 1.4 \times 10^{-13} A^{1/3}$ cm, we find $Q = 2.1 \times 10^{-24}$ cm^2. We will use this value of Q in evaluating the quadrupole interaction.

Since no magnetic hyperfine interaction is observed, the magnetic moment will not be calculated.

III. Experimental Procedures

The technique used in measuring the hyperfine structure was to measure the transmission of gamma rays from the source through a thin foil of resonantly absorbing material. Using the linear Doppler effect, the absorption lines are moved relative to the emission lines by moving the absorber toward and away from the source. When, at a certain speed, an absorption line coincides with an emission line, an absorption peak results.

A. Experimental Equipment

1. Velocity Spectrometer

The velocity spectrometer which provided the movement of the absorber consisted of a precision ground cam which converted rotary motion to linear to-and-fro motion. The different velocities required were obtained by changing the angular velocity of the cam with a gearbox. The velocity range covered was 0.088 cm/s to 10.0 cm/s in a total of 69 steps. This type of velocity drive has the advantages of being accurate, simple, and reliable.

The mechanical arrangement used is shown in fig. 4. The cam was made of hardened steel, bearing against flat hardened steel followers. The amplitude of the stroke was 1.9 cm, 1.7 cm of which represented the region of constant velocity. To reduce vibrations, the motors and gearboxes were mounted on a separate chassis from the cam mechanism.

The following tests have been performed to check on the accuracy and constancy of the velocity spectrometer:

a. Stroboscopically observing the rotation of the motor shaft, no dependence of the motor speed on the load was detected.

b. A static check of gear and cam linearity was made by measuring the carriage displacement as a function of motor shaft rotation, using a dial indicator. This indicated that the carriage was always within ± 0.001 cm of the correct position.

c. To check the proper behavior of the velocity spectrometer at high speeds, a velocity transducer was used. This measurement showed no variation greater than ± 0.1 cm/s at velocities up to 2 cm/s and no variations greater than ± 0.25 cm/s at velocities up to 10 cm/s.

These checks showed that any inaccuracies in the cam drive did not influence the experimental results.

Photoelectric gates restricted the measurement to those regions of the motion where the speed was constant. A light beam focused on a photomultiplier was interrupted by a sector attached to the cam. The photomultiplier output was used to gate the scalers. Two separate photoelectric gates were used to enable positive and negative velocities to be studied separately. The gates operated alternately; each gate was open 34% of the time, and closed the remainder of the time.

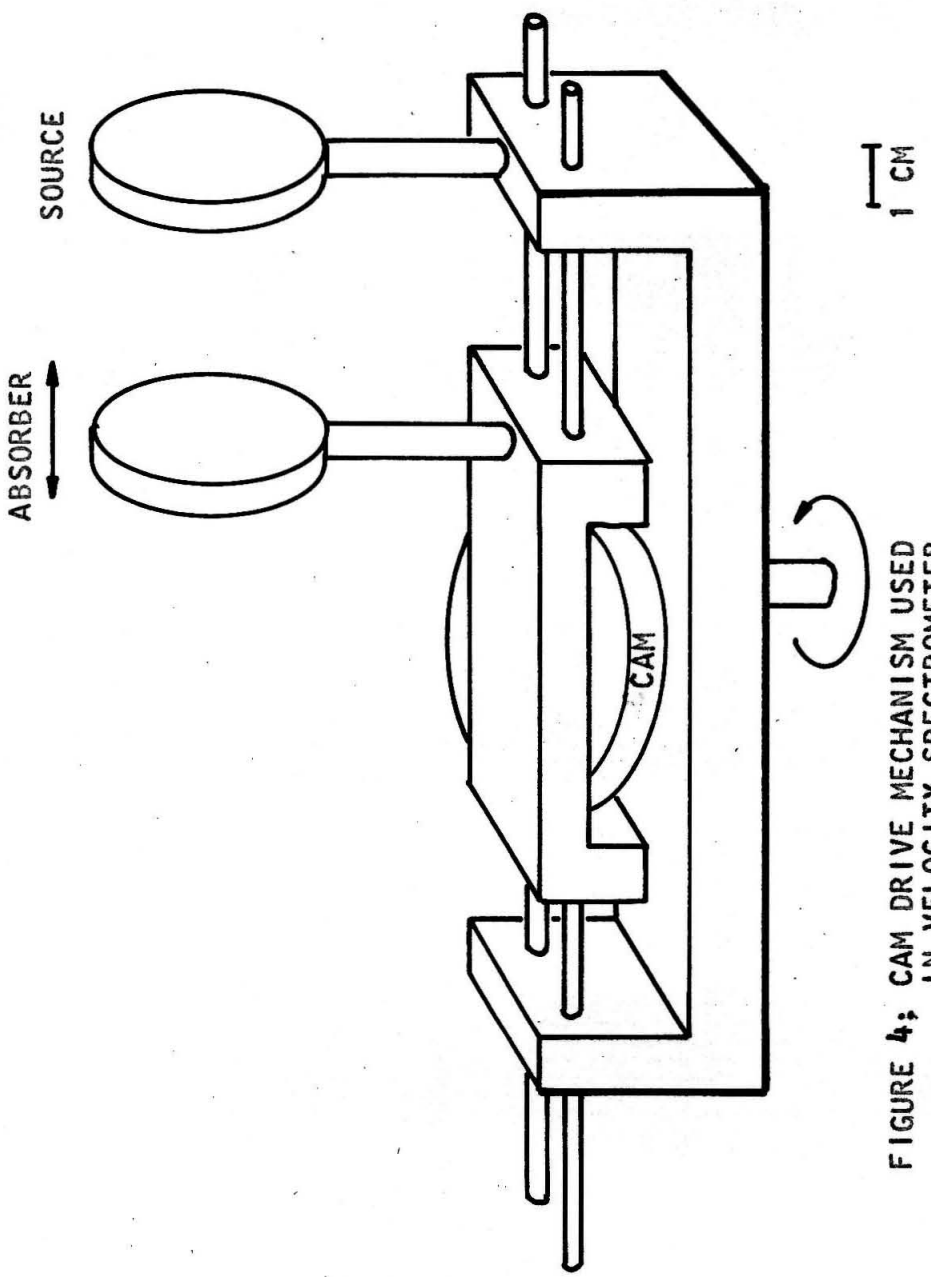

FIGURE 4: CAM DRIVE MECHANISM USED IN VELOCITY SPECTROMETER

2. Proportional Counters

Because of the extremely low energy of the transition being studied (8.4 kev), proportional counters were used to detect the gamma rays. These were built using an aluminum tube (40 cm long and 10 cm inside diameter) for the cathode, and a stainless steel wire (0.08 mm diameter) for the anode (see fig. 5). The ends of the aluminum cylinder were sealed off with Pyrex end plates which also supported the anode wire. The counter was filled with a mixture of 90% argon - 10% methane to a pressure of just under one atmosphere. The counter window was a 1 mm thick (200 mg/cm^2) beryllium disc 4 cm in diameter. Counters were assembled using an epoxy resin for fastening the end plates and the window, and then evacuated to a pressure of 10^{-5} mm before filling. After filling, the anode wire was electrically heated to improve the resolution. The resolution attained was about 17% at 6 kev, which is close to the theoretical limit. Unfortunately, this resolution was not good enough to resolve the 8.4 kev gamma-ray line from the thulium and erbium L X-ray complex present as a strong background. The spectrum shown in fig. 6 results from the composition of the 8.4 kev gamma ray and the L X-ray complex.

Due to the very high counting rates obtained (as high as 7×10^3 counts/second in the channel, and a total counting rate twice that), some precautions were necessary to prevent instability in the gas amplification and avoid rapid decomposition of the counting gas. The counters were run at a relatively low gas amplification of about 5×10^3 (high voltage about 2.2 kv), and then would count for about 10^{10}

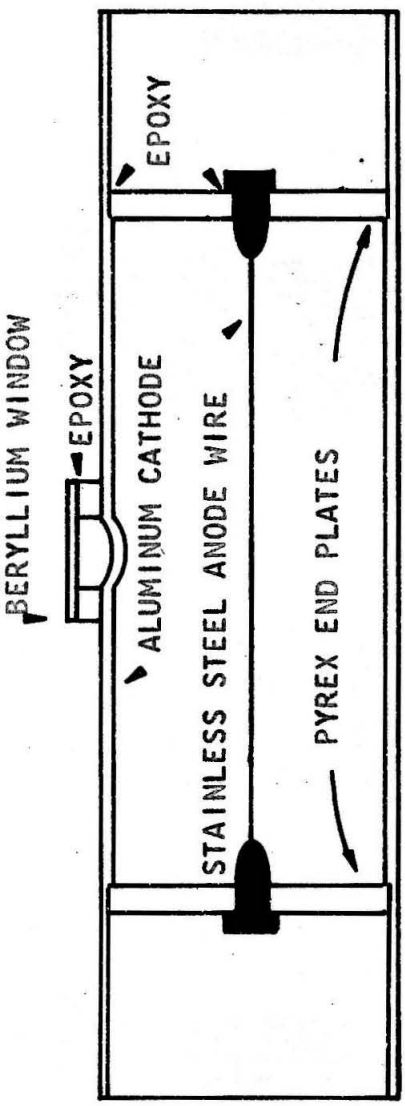

FIGURE 5: CROSS SECTION VIEW OF PROPORTIONAL COUNTERS USED

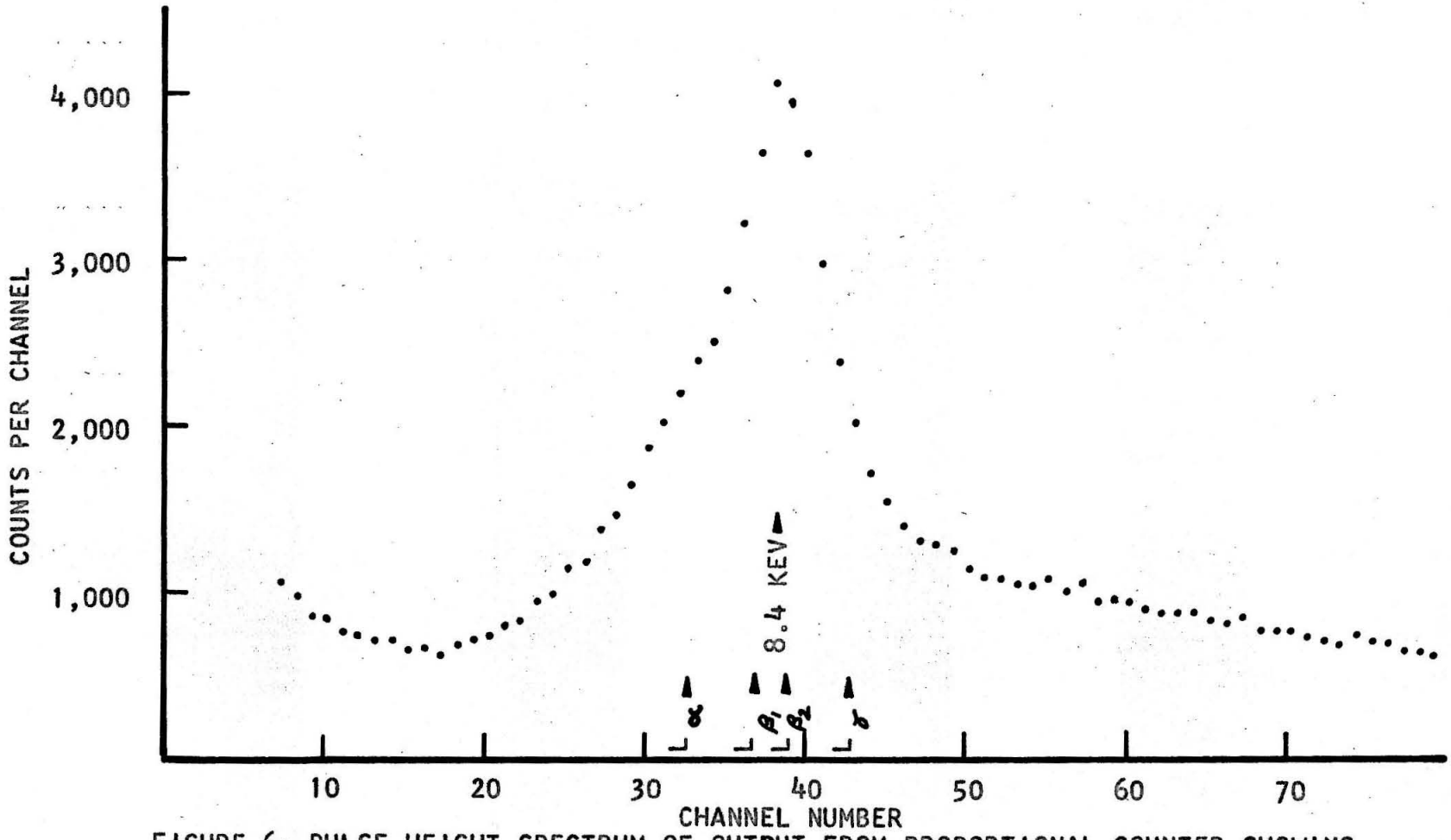

FIGURE 6: PULSE HEIGHT SPECTRUM OF OUTPUT FROM PROPORTIONAL COUNTER SHOWING THE COMPLEX SHAPE RESULTING FROM THE X-RAY BACKGROUND. THE POSITIONS CORRESPONDING TO THE ENERGIES OF THE STRONG ERBIUM L X-RAYS HAVE BEEN INDICATED.

counts before the resolution deteriorated seriously. At this point, heating the anode wire generally restored the original resolution; this process could be repeated several times before it was necessary to refill the counter. The output pulse was about 5 mv for an 8 kev gamma ray.

3. Electronics

A block diagram of the electronic equipment used is shown in fig. 7.

The signal from the counters was fed into a cathode follower preamplifier followed by a delay-line-clipped pulse amplifier and differential discriminator. The window of the differential discriminator was set appreciably wider than the actual width of the line being measured to minimize counting rate drift due to gain changes.

The pulses from the differential discriminator were counted by a transistorized multi-channel scaler with automatic print out. The scalers were controlled by the photoelectric gates. The signal from a 10 kc quartz-crystal-controlled oscillator was simultaneously gated and counted to determine the actual measuring time.

The measuring technique employed was to alternate runs of about 10 minutes with the absorber moving at 12 cm/s (a standardizing velocity high enough to eliminate resonance absorption) with runs of the same length at the measuring velocity v. The "Effect" as plotted in the figures was defined as

$$\frac{\text{(Count rate at 12 cm/s - count rate at v)}}{\text{Count rate at 12 cm/s}} .$$

The equipment was automatically controlled by a device which alternated standardizing and measuring runs and printed out the scalers at the end of the run.

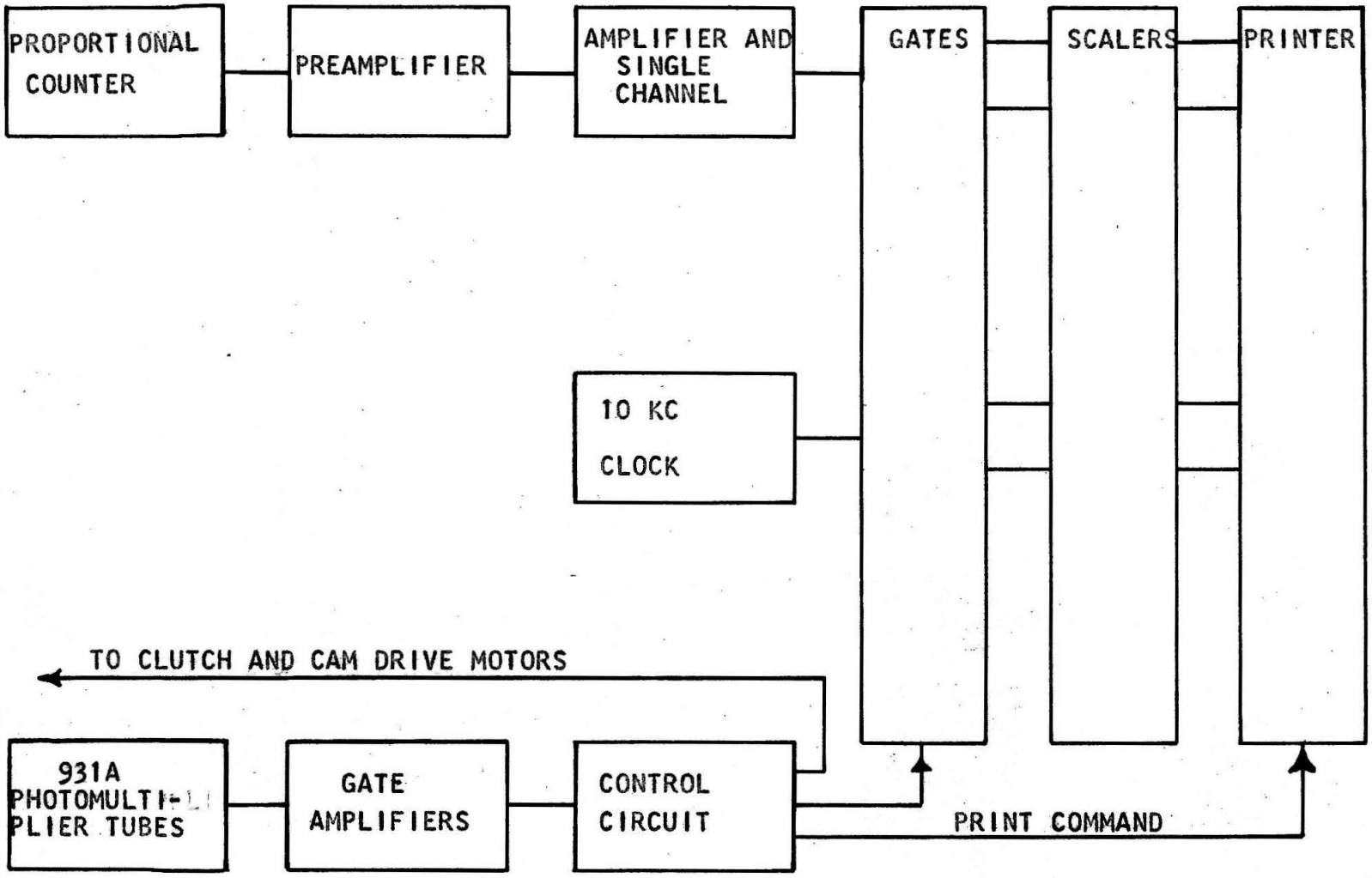

FIGURE 7: BLOCK DIAGRAM OF ELECTRONICS

4. Source Oven and Cryostat

The source temperature was varied from about 60° K to 1200° K during the present experiments. The temperatures below 300° K were attained by the use of a simple cryostat with dry ice or liquid nitrogen as a refrigerant. Beryllium windows were used to transmit the gamma rays. Temperatures below the boiling point of nitrogen (77° K) were attained by pumping on the nitrogen; in this range the temperature was controlled by a pressure activated switch that measured the vapor pressure of the nitrogen and actuated a solenoid valve in the pumping line.

The source heater used is shown in fig. 8. It had the advantage of having the heating element isolated from the source, so that the atmosphere on each could be controlled separately to minimize chemical reactions. By using both bifilar and ordinary winding of the Kanthal heating coil, it was shown that the magnetic field due to the heating current, a maximum of 50 gauss, had no influence on the pattern of source lines. The oven temperature was controlled to a few degrees and monitored by a thermocouple.

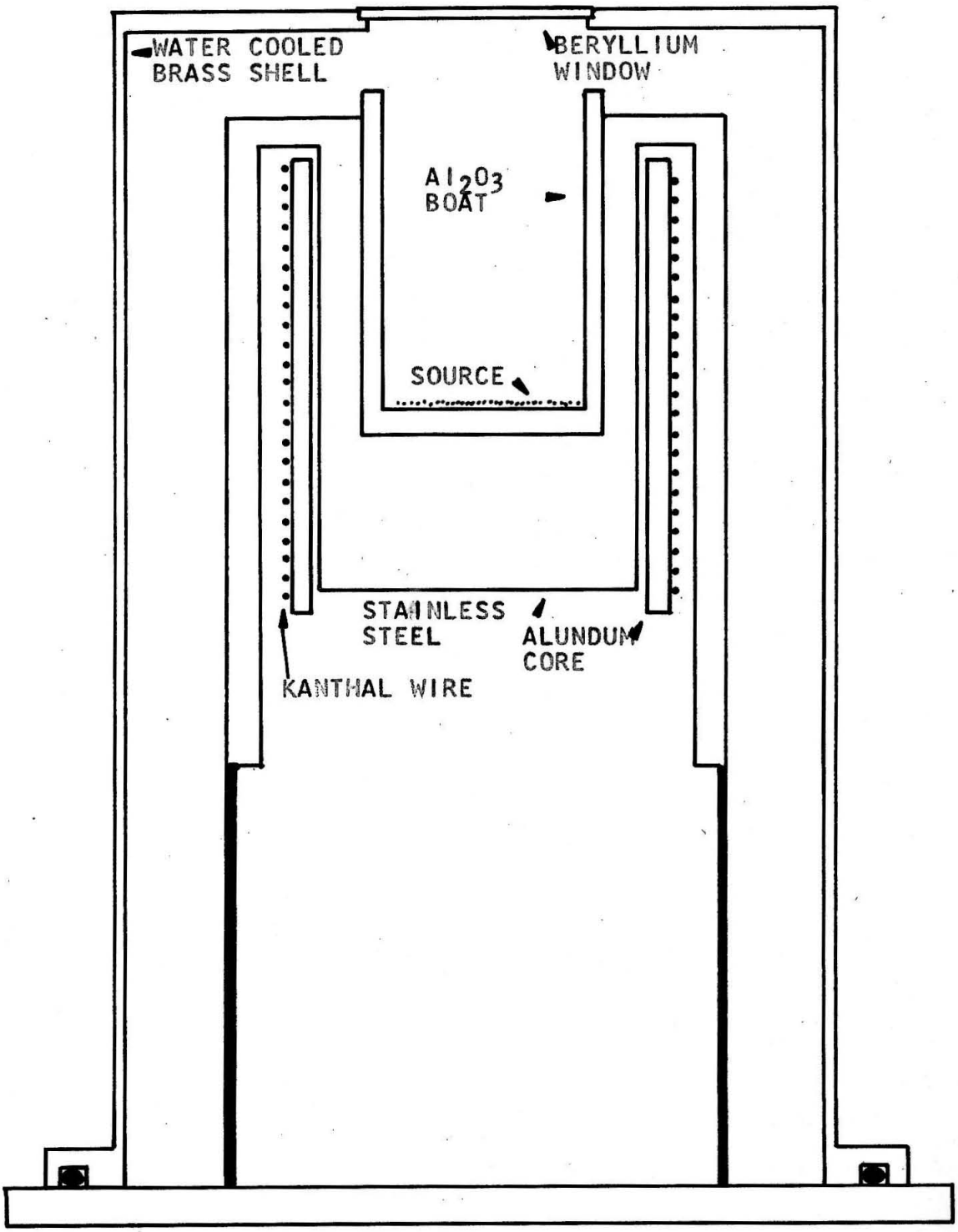

FIGURE 8: SOURCE OVEN USED AT TEMPERATURES TO 1300 K

B. Preparation of Sources and Absorbers

1. Source Preparation

Sources were produced by irradiating natural erbium metal and oxide for three weeks in a flux of 5×10^{14} N/cm^2/s in the Materials Testing Reactor at Idaho Falls, Idaho. The specific activity obtained was usually on the order of 10 C/g. Sources of about 20 mg. were used, resulting in a counting rate of about 3,000 (gamma rays plus L X-rays)/second in the channel, after the attenuation by windows and the absorber photoabsorption. The strong internal conversion of the 8.4 kev transition required relatively high source activity to get useful gamma counting rates.

Since the experiment is primarily a study of the interaction of the nuclear quadrupole moment with the electric field gradient depending on the crystal lattice symmetries, the effects of the radiation damage to the lattice from the reactor irradiation had to be taken into account. To eliminate these effects, the oxide sources were chemically processed after irradiation. They were dissolved in acid, precipitated as erbium oxalate, and then heated in oxygen to form the oxide. Metal sources were made either by vacuum evaporation at a pressure of 10^{-5} mm Hg or better, or from irradiated metal filings with no post-irradiation treatment. This procedure was justified because the types of radiation damage caused by thermal neutron irradiation and subsequent gamma radiation would be expected to be annealed out at room temperature in the metal.

Sources were usually mounted on beryllium discs about 1 mm thick and 4 cm in diameter. Powder sources (metal and oxide) had to be spread very uniformly to minimize the effects of self-absorption; they were held in place with a coating of paraffin or by clamping with a beryllium cover disc. Beryllium was particularly useful for source holders because the low Z allowed the transmission of the 8.4 kev with only small attenuation and gave little bremstrahlung in stopping the electrons resulting from the beta decay.

Sources of mixed $(Tm\text{-}Y)_2O_3$ were made by dissolving the active material and the yttrium together in acid, precipitating the mixed oxalate, and heating in the same way as the pure Er_2O_3 sources.

2. Absorber Preparation

The resonance absorption cross section was approximately 7×10^{-19} cm^2/atom (see eq. 1). Taking into account line broadening effects and photoabsorption, the most useful absorber thickness was in the range of 2-5 mg/cm^2. It was possible to make uniform layers of thulium oxide and garnet in this thickness range by allowing a suspension of the powdered compound in an organic solvent to settle onto a beryllium disc. The same disc then served as the support for the absorber, since it was rigid and transparent to the gamma rays. The powder was covered with a thin layer of paraffin for mechanical stability and protection against atmospheric humidity. The coating made no noticeable difference in the observed absorption spectrum.

Metal absorbers were made by evaporating thulium metal from a tantalum or tungsten filament onto a beryllium backing disc. It was necessary to etch the beryllium slightly to make the thulium layer adhere. Pressures from 10^{-5} to 10^{-7} mm were maintained during the evaporation, and a shutter was used to prevent deposition during the outgassing procedure and the first part of the evaporation. Since the evaporation was done by subliming the thulium from the solid state, contamination by the boat material was not a problem. There was a noticeable improvement in the sharpness of the absorption lines when the pressure during evaporation was lowered from 10^{-5} mm Hg to 10^{-6}, but further improvement to 10^{-7} made no observable difference.

Attempts to anneal the metal absorbers to improve the crystal structure of the thulium layer resulted in very bad smearing

of the absorption spectrum, probably due to diffusion of the beryllium backing into the thulium.

Absorbers of thulium diffused into copper (similar to those used by Ofer (3)) were made by vacuum evaporation of thulium onto a clean copper foil, heating the combination for preliminary annealing without breaking the vacuum, and then annealing in a pure hydrogen atmosphere for 12 hours at 960° C. This amount of heating was not sufficient to distribute the thulium through the copper with perfect uniformity, but at least some had diffused completely through the copper.

IV. Results

The ground state of Er^{169} produced by neutron irradiation decays to the 8.4 kev state in Tm^{169}. Thus the source consists of radioactive thulium ions in a surrounding of erbium ions. The local surrounding of the thulium ions in source and absorber is therefore different.

This difference can be neglected in interpreting the results of the present experiment because of the chemical similarity of these two elements. No experimental evidence was found for a different hyperfine structure in source and absorber under equivalent conditions.

A. Measurements at Room Temperature

1. Oxide Source and Absorber

Figure 9 shows the transmission observed as a function of velocity between an Er_2O_3 source and Tm_2O_3 absorber. According to Part II, the pattern can be explained in the following way: For ions in physically equivalent lattice sites, the nuclear emission line is symmetrically split into two components of equal intensity. The split is produced by the quadrupole interaction only, since the magnetic interaction is cancelled by the spin-lattice relaxation phenomenon. The nuclear absorption line is similarly split into two components.

The relative position of emission and absorption lines is illustrated in fig. 10 assuming identical splittings in source and absorber. The resonance absorption should be the strongest at zero relative velocity between source and absorber, since each emission line coincides with an absorption line. If the splitting between the lines is ΔE, and if we move the absorber toward or away from the source with velocity $v = c \frac{\Delta E}{E_o}$, we obtain side peaks of one-half the intensity of the central peak which result from a coincidence between one emission line and one absorption line. In this way, we obtain the three peak pattern of fig. 9.

The explanation above neglects the fact that in Tm_2O_3 the Tm ions appear in two physically inequivalent sites, in the ratio of three Tm ions in sites with C_2 symmetry for each Tm ion in a site with C_{3i} symmetry. We obtain two quadrupole doublets in the intensity ratio

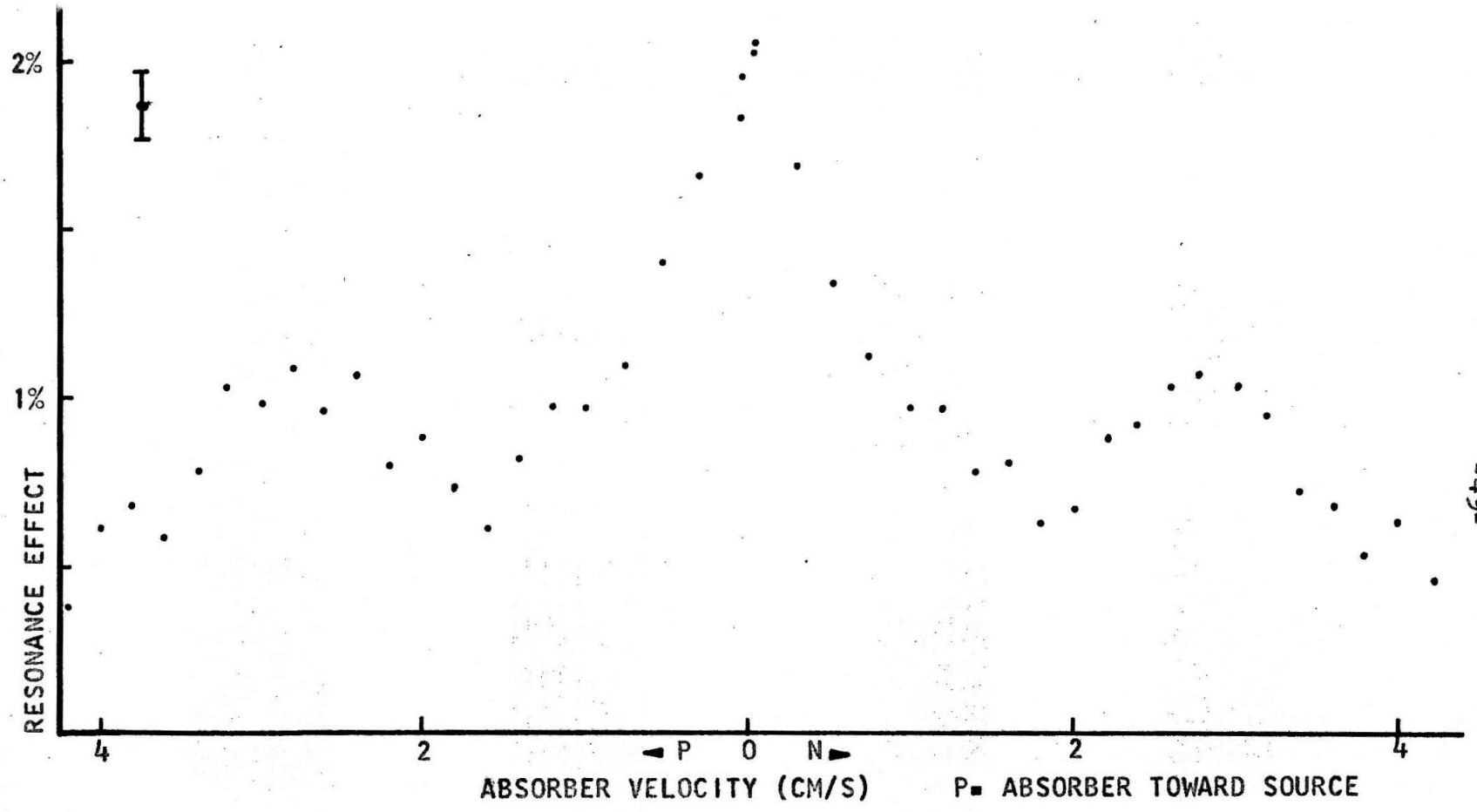

FIGURE 9: PATTERN OF RESONANCE ABSORPTION OBSERVED WITH OXIDE SOURCE AT 300 K AND OXIDE ABSORBER AT 300 K.
RESONANCE EFFECT IS DEFINED AS $\frac{\text{COUNTING RATE AT 12 CM/S - COUNTING RATE AT V}}{\text{COUNTING RATE AT 12 CM/S}}$

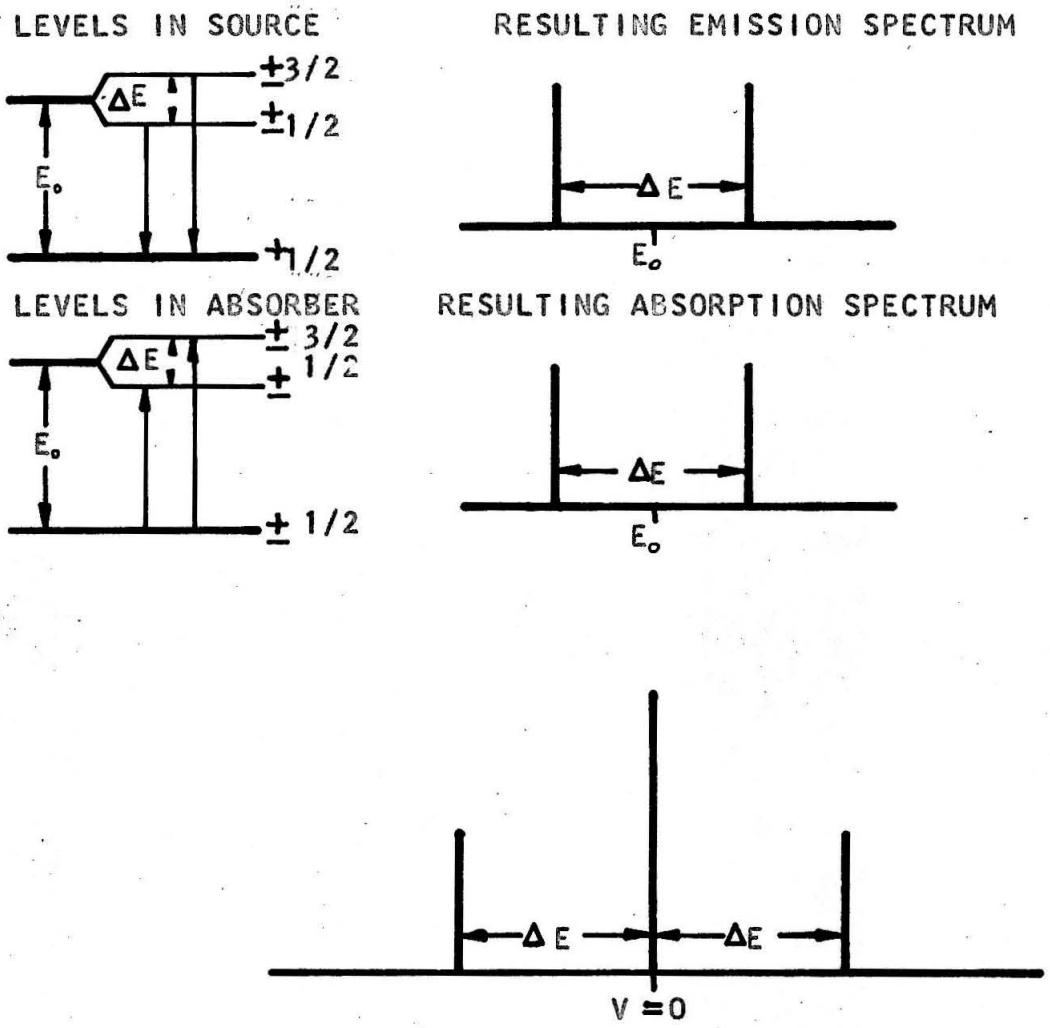

OBSERVED ABSORPTION PATTERN RESULTING FROM EMISSION AND ABSORPTION SPECTRA SHOWN

FIGURE 10: EXPLANATION OF 3 PEAK PATTERN SHOWN IN FIG. 9

3:1 from these two lattice sites. In the presence of the strong peaks, the weak peaks resulting from the less populated sites have not been observed, and we will neglect their existence in the interpretation of the experimental results.

2. Metal Source and Absorber

If the source and absorber are erbium and thulium metal, respectively, the resultant hyperfine pattern is completely different from that of the oxide source and absorber. The observed pattern (see fig. 11) shows that in both source and absorber, any hyperfine splitting is small compared to the line width observed. This shows that the field gradient at the nuclei in the metal (symmetry D_{3h}) is much weaker than that in the oxide.

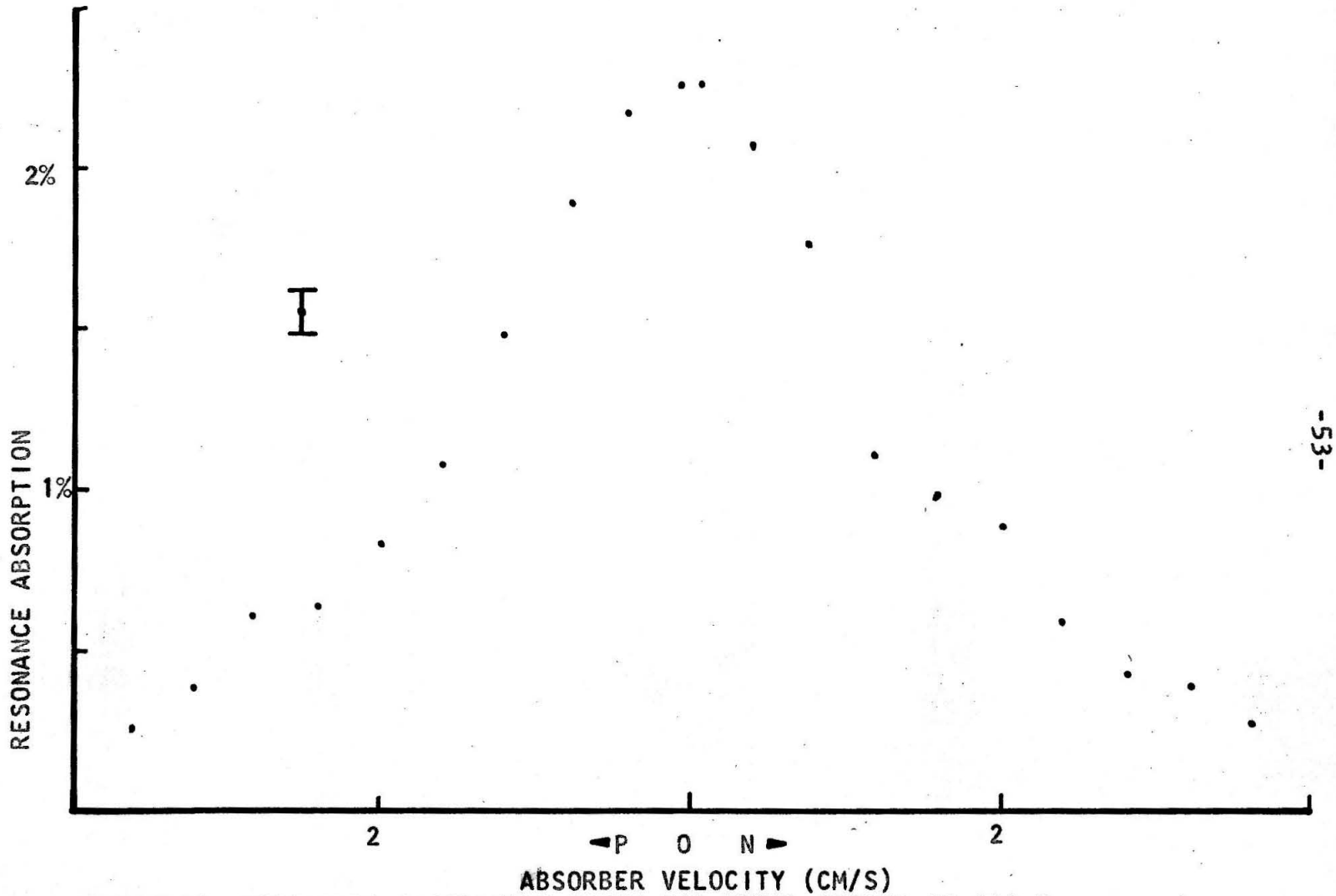

FIGURE 11: RESONANCE ABSORPTION CURVE FOR METAL SOURCE AT 300 K
ABSORBER: METAL AT 300 K

3. Metal Source and Oxide Absorber

Correspondingly, if a metal source is used with an oxide absorber (or vice versa), the moving of the single line of the metal over the two lines of the oxide results in an absorption pattern of two peaks (see fig. 12), with the same energy separation as in fig. 9, representing the quadrupole splitting in the oxide absorber.

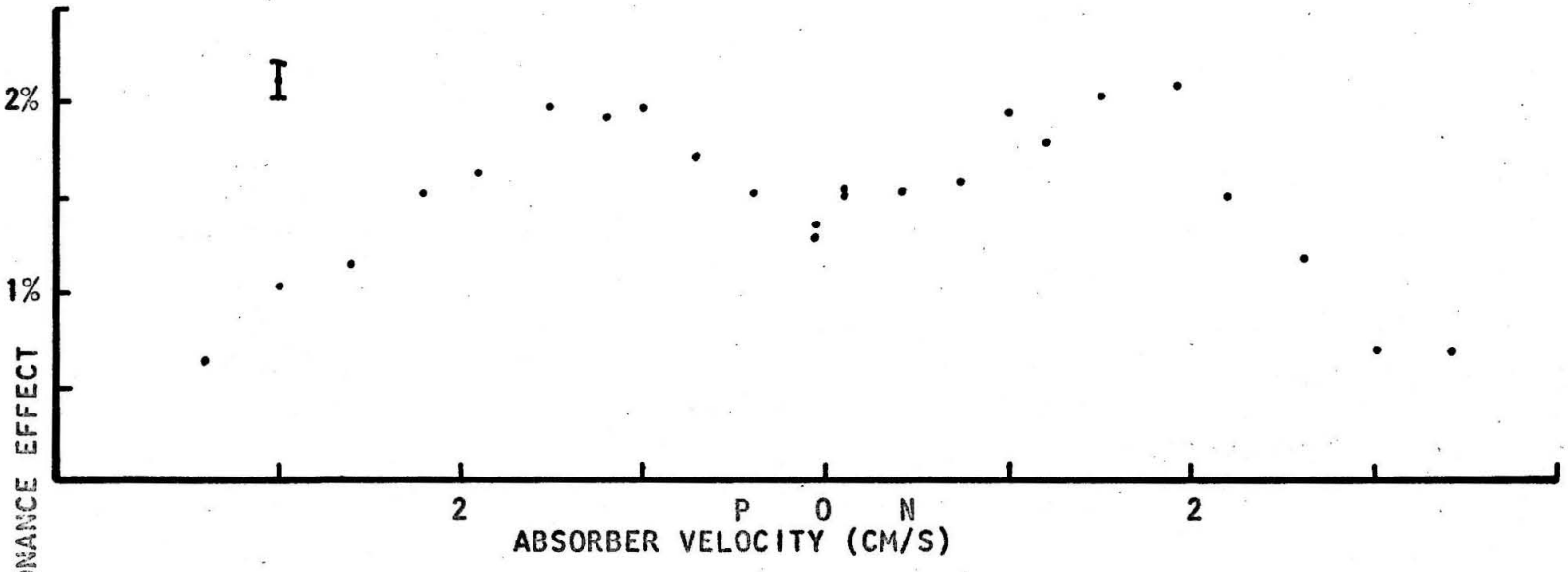

FIGURE 12: RESONANCE ABSORPTION PATTERN OBSERVED USING OXIDE SOURCE AT 300 K AND METAL ABSORBER AT 300 K

4. Studies of Other Absorbing Materials

In the same fashion, the absorption spectra of various other materials were studied using metal and oxide sources.

For example, an absorber of thulium diffused into copper in the ratio 1:30 (atomic) was studied. The absorption spectrum of this absorber taken with a source emitting an unsplit line is shown in fig. 13. Though the pattern resembles that of an oxide absorber, it is believed to result from the quadrupole interaction of thulium ions in copper. It is not yet known whether the thulium ion appears as a replacement for a copper ion, an interstitial, or in a binary alloy with the copper.

In another experiment, a preliminary run using an absorber of thulium ethyl sulfate showed no resonance absorption. The reason for this is not yet known, but the material merits further study since it would be useful in tying together the results of Mössbauer experiments, paramagnetic resonance, and optical spectroscopy.

In an effort to determine the magnetic moment of the excited state of Tm^{169}, several runs were made using thulium iron garnet, which is ferrimagnetic at room temperatures. A strong resonance composed of several lines was obtained (fig. 14), but the resolution was not good enough to decompose the pattern. As many as eight lines were expected under the influence of the nuclear Zeeman splitting and quadrupole shifts.

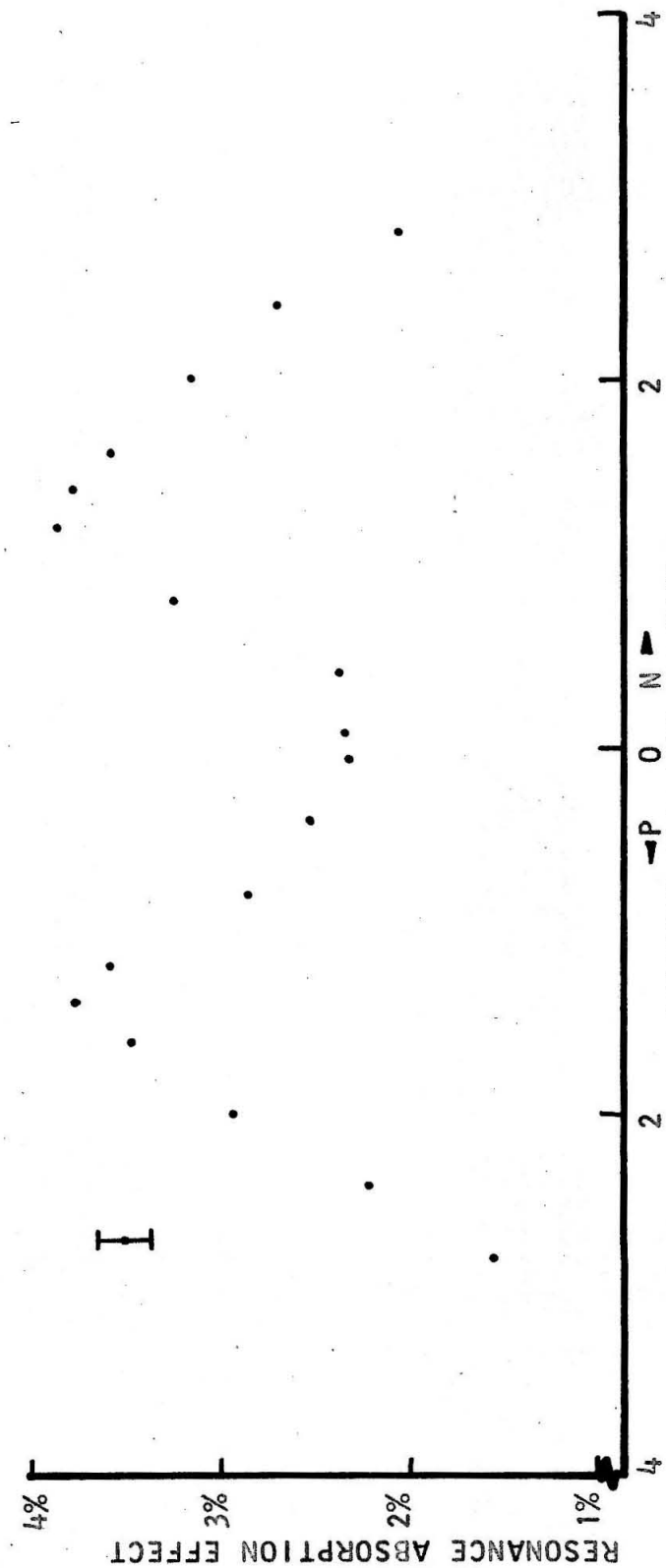

FIGURE 13: ABSORPTION SPECTRUM OF THULIUM DIFFUSED INTO COPPER SOURCE: UNSPLIT LINE FROM ERBIUM OXIDE AT 700 K

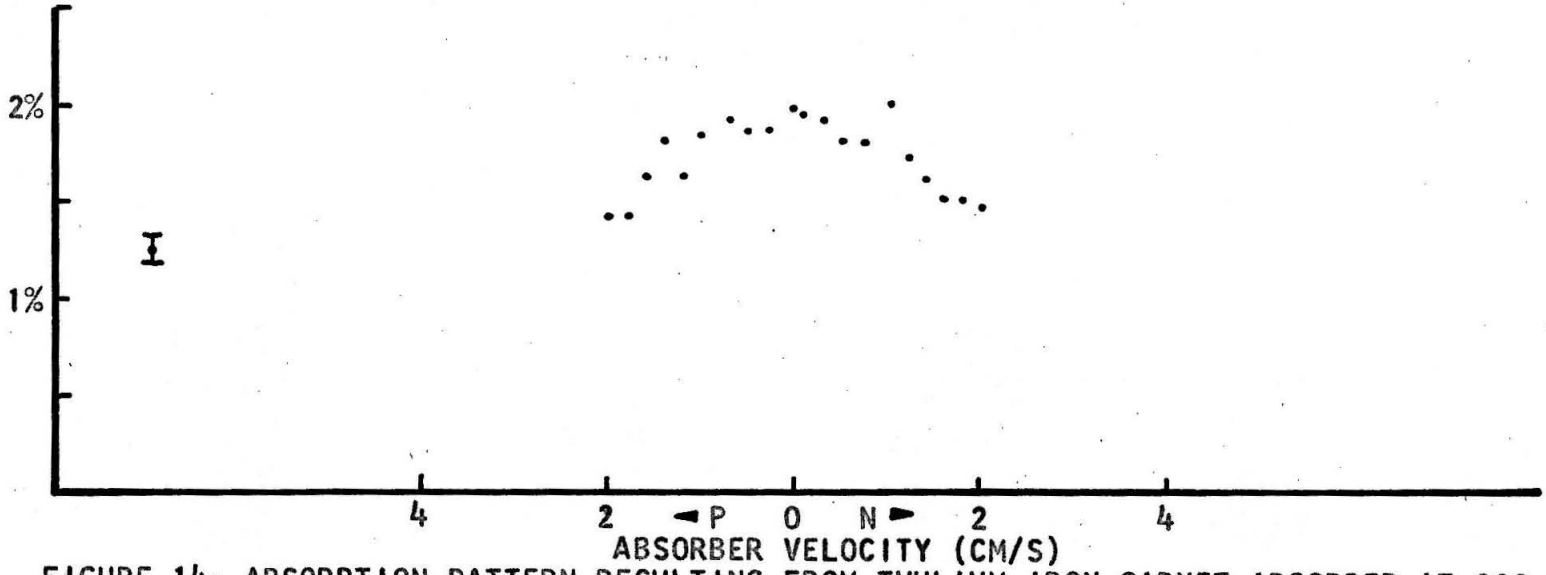

FIGURE 14: ABSORPTION PATTERN RESULTING FROM THULIUM IRON GARNET ABSORBER AT 300 K SOURCE METAL AT 300 K

B. Measurements Above and Below 300° K

Figures 15, 16 and 17 show a selection of experimental results with an absorber of Tm_2O_3 at 300° K and a source of Er_2O_3 at temperatures from 77° K to 1230° K. The figures demonstrate the strong temperature dependence of the quadrupole splitting. Figure 18 shows the temperature dependence of the quadrupole splitting obtained by the analysis of all the measurements with oxide sources and oxide and metal absorbers.

Using metal sources, no splitting was resolved at room temperature or above, but a splitting was observed at 77° K (fig. 19). Below 77° K, the resonance absorption disappeared almost completely.

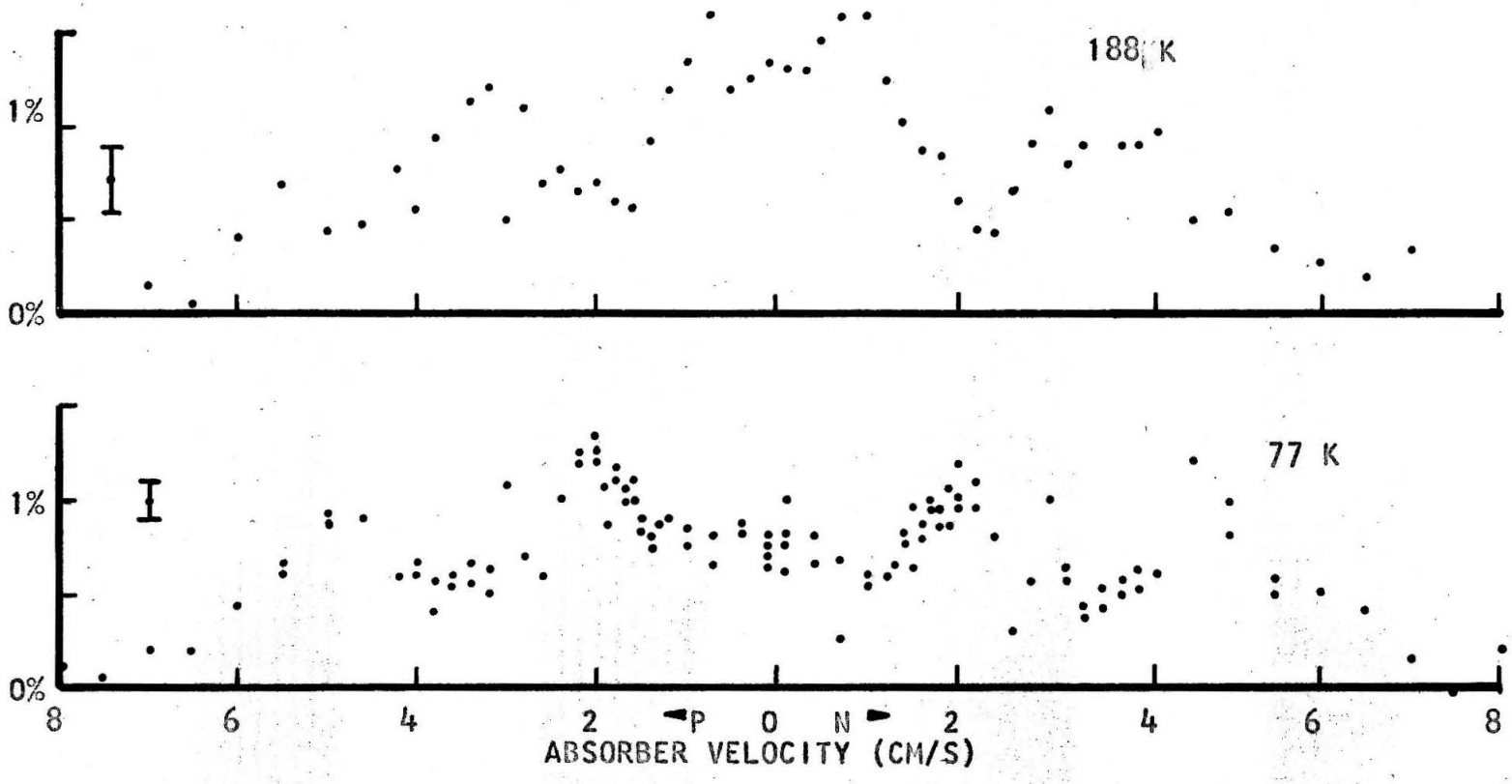

FIGURE 15: ABSORPTION PATTERN RESULTING FROM OXIDE ABSORBER AT 300 K AND OXIDE SOURCE AT TEMPERATURES SHOWN

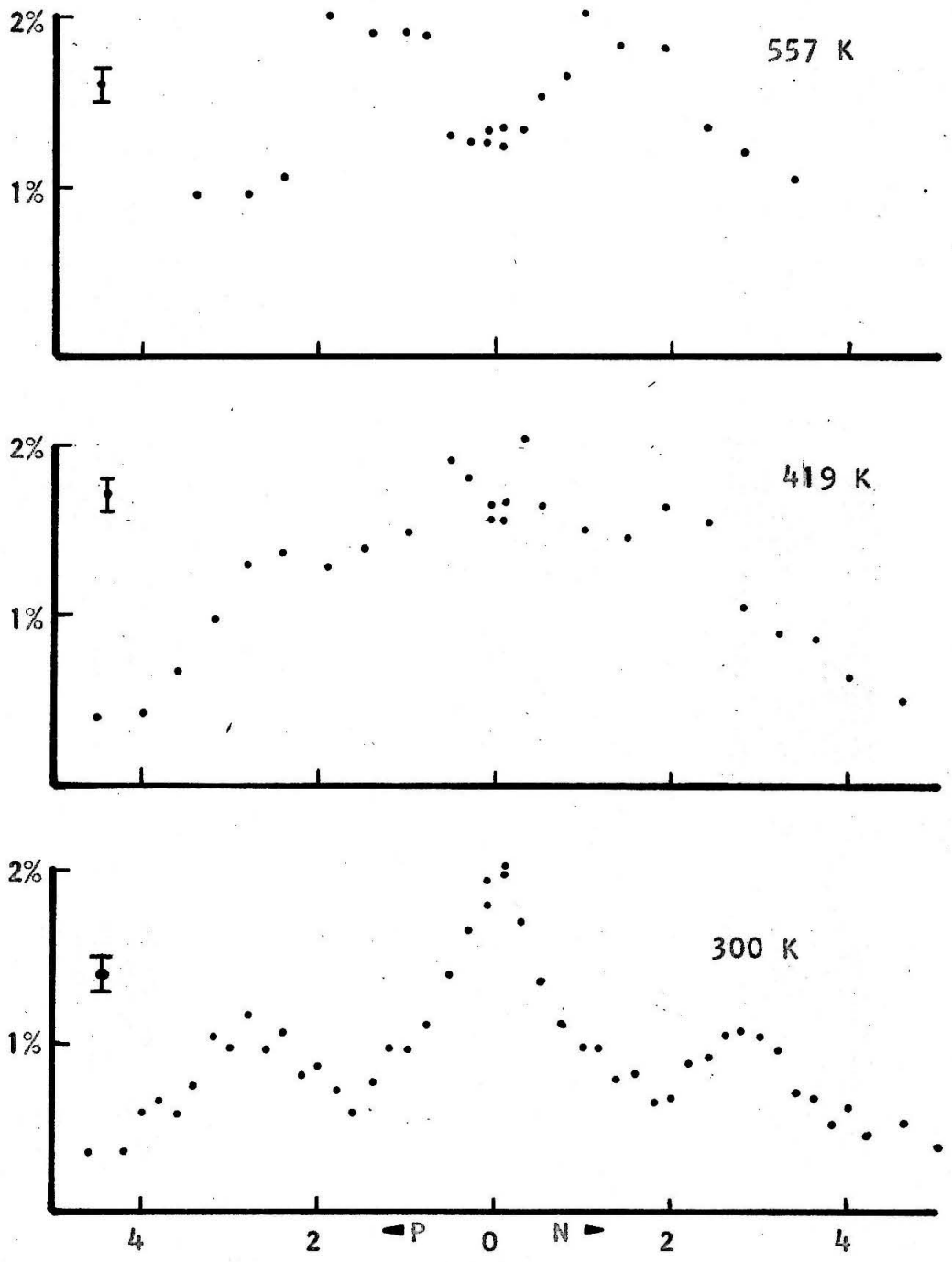

FIGURE 16: ABSORPTION PATTERNS RESULTING FROM OXIDE ABSORBERS AT 300 K AND OXIDE SOURCES AT TEMPERATURES SHOWN IN FIGURE

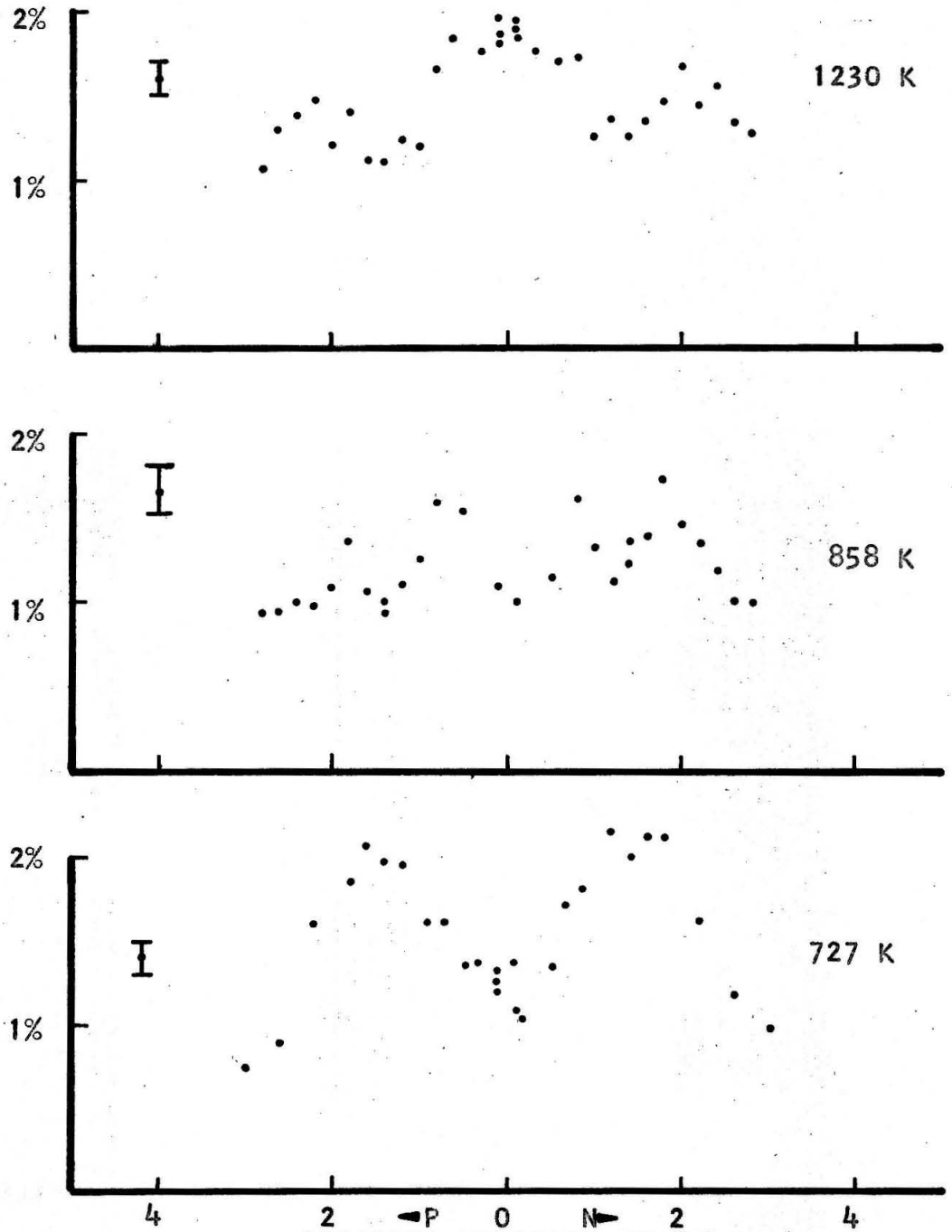

FIGURE 17: ABSORPTION PATTERNS RESULTING FROM OXIDE ABSORBERS AT 300 K AND OXIDE SOURCES AT TEMPERATURES SHOWN IN FIGURE

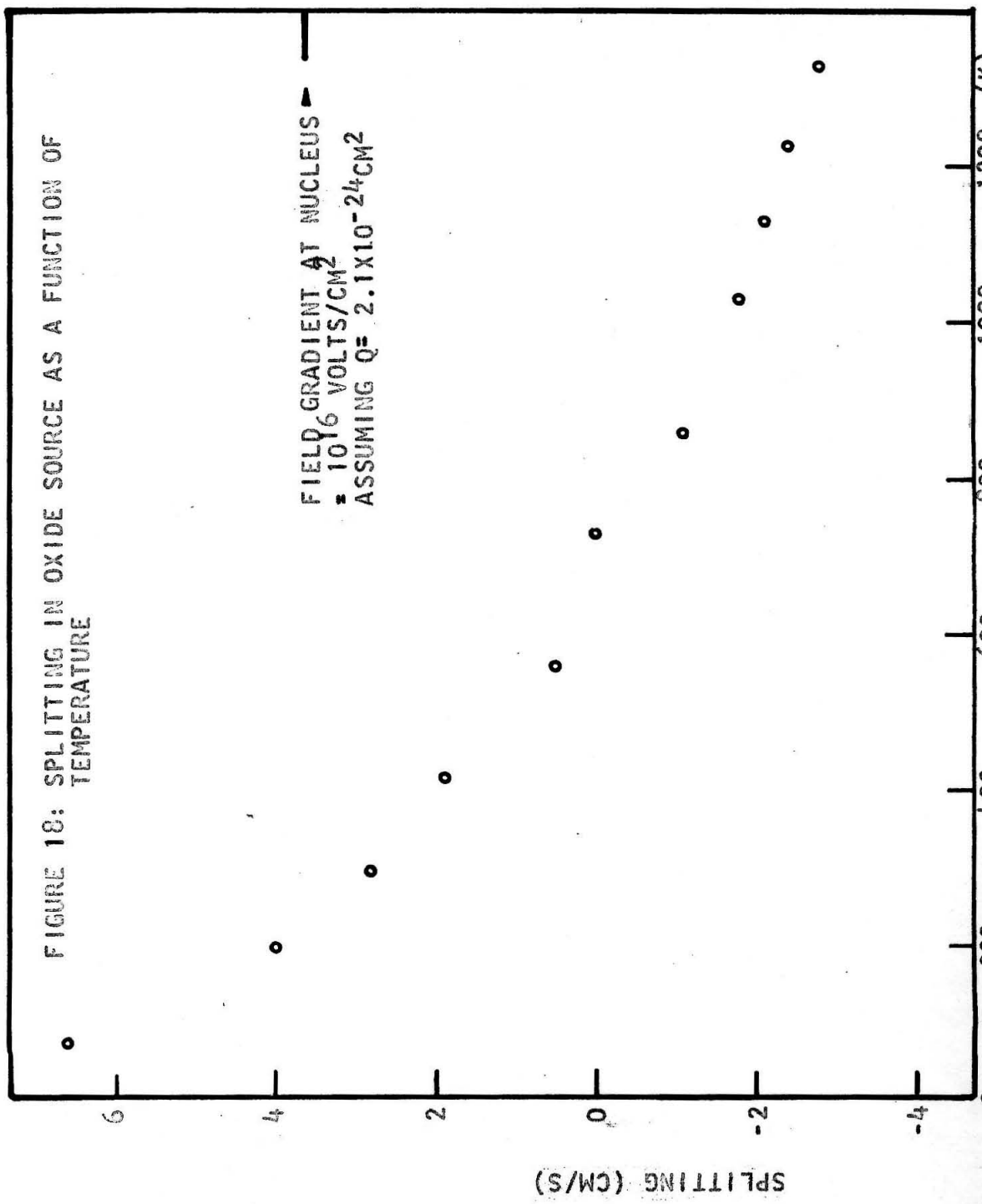

FIGURE 18: SPLITTING IN OXIDE SOURCE AS A FUNCTION OF TEMPERATURE

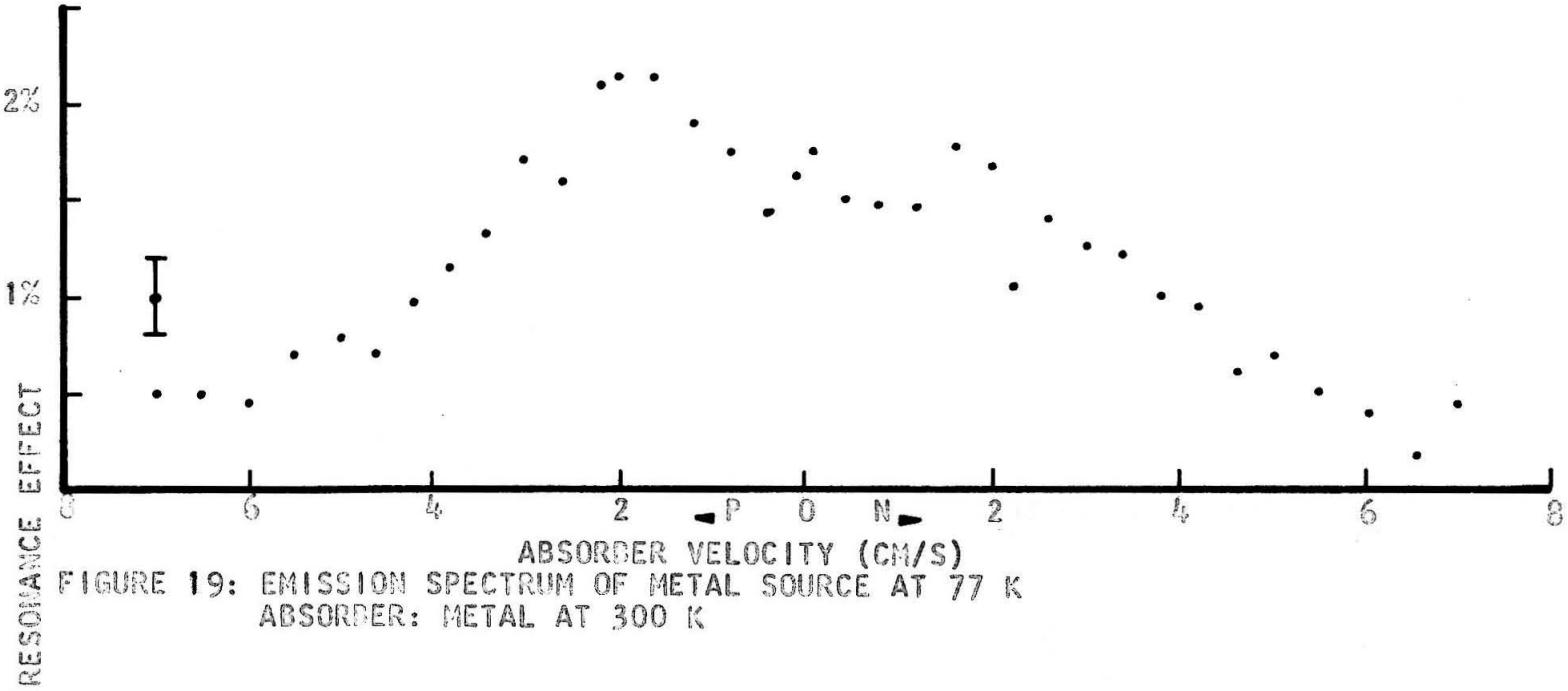

FIGURE 19: EMISSION SPECTRUM OF METAL SOURCE AT 77 K
ABSORBER: METAL AT 300 K

V. Discussion

A. The Magnitude and Temperature Dependence of the Hyperfine Structure

The analysis of the hyperfine interaction in Part II showed that the quadrupole interaction is the only important source of hyperfine splitting in most of the present experiment. It was also shown that the field gradient which produces the quadrupole splitting has two significant sources: $\gamma\nabla\vec{E}'$, the antishielding of the crystal field gradient by the closed shells, and $\overline{\nabla\vec{E}''}$, the field gradient generated by the 4f electrons, so that $\overline{\nabla\vec{E}} = \overline{\nabla\vec{E}''} + \gamma\nabla\vec{E}'$. $\overline{\nabla\vec{E}''}$ cannot be calculated as a function of temperature and crystal symmetry with the present limited knowledge of particular crystal field and electronic splittings. However, the maximum possible value of $\overline{\nabla\vec{E}''}$ can be easily calculated. The 4f electronic wave function giving the largest field gradient at the nucleus is the one containing only $m_j = \pm 6$. Using the set of equations on pages 22 and 23, and the notation of page 8, we obtain:

$$\phi_{zz} = eq = 2e\langle r^{-3}\rangle \cdot \frac{4}{3\cdot 5} \qquad \text{and} \qquad \eta = 0.$$

From equations 5a and 5b,

$$\Delta E = \frac{(3+3)\, e^2qQ}{12}\left(1+\eta^2/3\right)^{1/2},$$

and using $Q = 2.1 \cdot 10^{-24}$ cm^2 and $\langle r^{-3}\rangle = 7.1 \cdot 10^{25}$ cm^{-3} (15, 16) $\Delta E = 5 \cdot 10^{-6}$ ev = 18 cm/s. This estimate of the maximum quadrupole interaction resulting from the 4f electrons only is entirely independent of the crystal symmetry. The accuracy should be within $\pm 20\%$, with

the major part of the uncertainty coming from the estimate of Q from the Nilsson model.

$\gamma\nabla\vec{E}'$, the temperature independent component of the field gradient, produces the second contribution to the quadrupole splitting. It depends primarily on the crystal symmetry. We can make a crude estimate of $\gamma\nabla\vec{E}'$ for Tm_2O_3 from a model that consists of a thulium ion halfway between two O^{2-} ions 4.6 Å apart. Using an antishielding factor $\gamma = -100$, the resultant splitting is 10^{-5} ev = 36 cm/s.

The curve of fig. 18 shows that the splitting varies from 6.6 cm/s at 77° K to -2.8 cm/s at 1330° K. At 680° K the effective gradient passes through zero within the experimental accuracy, showing that $\gamma\nabla\vec{E}' \approx -\overline{\nabla\vec{E}''}$. The total variation of the splitting with temperature is 9.4 cm/s, well within the maximum predicted from the 4f electronic wave functions. The temperature independent part of the splitting is about an order of magnitude smaller than the result of the crude calculation above.

In the metal source, the total quadrupole splitting appears to be small compared to the oxide case. This can probably be accounted for by the higher symmetry of the metal crystal, which makes $\overline{\nabla\vec{E}'}$ very small and decreases E_1, the splitting of the electronic levels. The relatively small splitting of the electronic levels in the metal allows the spin-lattice relaxation averaging process (see page 17) to cancel the field gradient from the 4f electrons even at 300° K, resulting in an unsplit line at room temperatures.

The disappearance of resonance absorption below 77° K can be attributed to the fact that erbium metal is antiferromagnetic below 78° K, resulting in very complex patterns. This distributes the intensity of the lines over so many peaks that the resonance absorption becomes undetectable.

B. Size of the Resonance Effect

The relatively weak strength of the resonance effect, only a few percent for all source and absorber combinations, is due to a strong background of X-rays which have approximately the energy of the gamma line.

The most important contribution to the X-ray background comes from the ionization of erbium L shell electrons by the 300 kev electrons resulting from the beta decay of the Er^{169}. Since there are about 200 betas produced for each 8.4 kev gamma ray and each beta can produce several L shell ionizations, a strong X-ray background arises. In addition, the 8.4 kev gamma ray line is energetic enough to be critically absorbed in the L_{III} shell of erbium in the source, with L X-rays resulting.

The use of thin and uniform sources was effective in reducing the X-ray background, thereby enhancing the resonance effect.

C. Line Widths

The natural line width, Γ, calculated from the recently measured half-life of 6.9 ns (17), is 0.2 cm/s. In the present experiment, a source line having width Γ is moved over an absorption line of width Γ, resulting in a total width of 2Γ in the absorption pattern measured as a function of relative velocity between source and absorber. However, the actually observed line widths have been at least six times this value.

There are three likely causes for line broadening in the present experiments:

a. excessive absorber thickness

b. lattice imperfections and chemical impurities in the source and absorber compounds

c. imperfect averaging over the electronic states by the spin-lattice process.

These effects will be discussed in the above order.

a. Figure 20 shows curves of peak resonance absorption and measured line width as a function of absorber thickness. The results of a theoretical calculation of line broadening as a function of absorber thickness are plotted on the same scale.

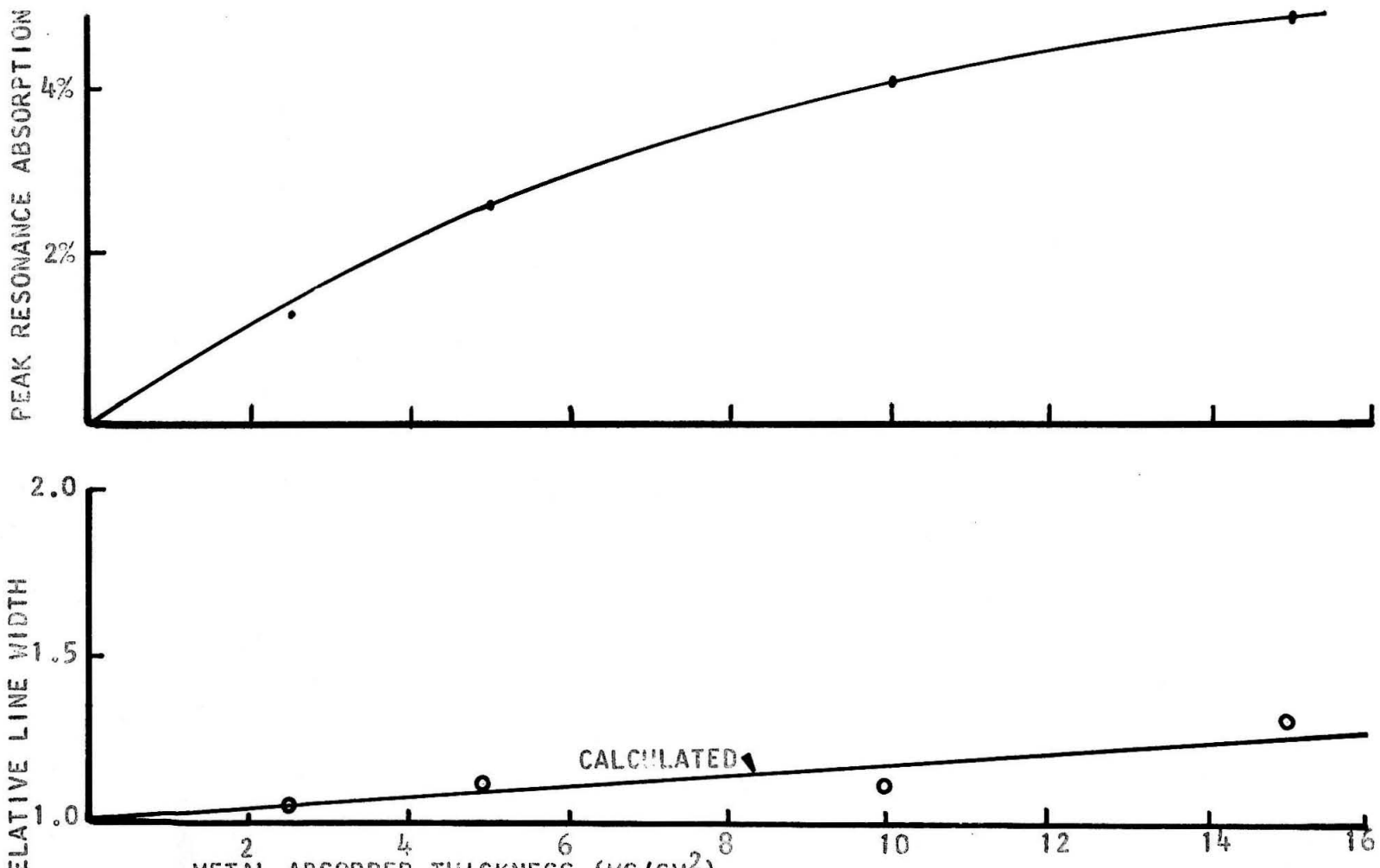

FIGURE 20: PEAK RESONANCE ABSORPTION AND RELATIVE LINE WIDTH AS A FUNCTION OF ABSORBER THICKNESS. SOURCE: METAL

From these curves it is apparent that absorber thicknesses in the range 2-5 mg/cm^2 do not appreciably broaden the observed pattern.

b. Lattice imperfections, however, were definitely established to be significant as a cause of line broadening since the line widths observed showed a dependence on the preparation technique of sources and absorbers. In metal sources and absorbers made by vacuum evaporation, the line width decreased noticeably when the pressure during the evaporation was reduced, but there was no further improvement in using pressures below 10^{-6} mm Hg. Attempts to anneal the evaporated films to improve the crystal structure have failed to date because of the diffusion of the thulium metal into the backing material. Experiments to produce unsupported metal films are now in progress. In oxide source and absorber materials, the ultimate line width achieved by various physical and chemical treatments was 2.4 cm/s, corresponding to a broadening by a factor of 6. Considerable care was taken to prevent decomposition and diffusion of the Er_2O_3 sources at elevated temperatures. The use of boats of Al_2O_3 in an atmosphere of pure nitrogen resulted in stable and reproducible spectra.

No line broadening from radiation damage was expected after chemical treatment of the oxide sources.

c. The remaining cause of the observed line broadening is then that the spin-lattice relaxation time is not fast enough to average the magnetic and quadrupole splitting

perfectly. A broadening from this cause is very difficult to estimate, since the relaxation times, supposedly about 10^{-12} s in the metal at 300° K, are not precisely known. (The spin-lattice relaxation times in thulium ethyl sulfate are known to be 10^{-6} at 4° K (18).)

The spin-lattice relaxation time increases sharply with decreasing temperature, and the line broadening observed at low temperatures (see figs. 15 and 19) may be due to a breakdown of the averaging process at these temperatures.

VI. Summary

The recoilless resonance absorption of the 8.4 kev gamma ray emitted from Tm^{169} has been observed. Using this resonance, the hyperfine splitting of the nuclear energy levels in Tm^{169} has been studied in source and absorber materials of various chemical compositions in a temperature range from 65° K to 1330° K.

Arguments based on the fundamental properties of the Hamiltonian of the rare earth ion in the crystal electric field and on the electron spin-lattice relaxation phenomenon have been presented to show that there is no magnetic hyperfine interaction under most conditions.

The quadrupole contribution to the hyperfine interaction was studied both theoretically and experimentally, with particular emphasis on the variation of the quadrupole splitting with temperature.

It was shown that at certain temperatures the quadrupole splitting could be eliminated, so that an unsplit line resulted. This procedure makes it possible to produce sources of rare earth ions emitting an unsplit line without the use of a cubic surrounding, which is difficult to obtain with the 3+ rare earth ions. The use of a source emitting an unsplit line greatly simplifies the interpretation of the absorption patterns by allowing the direct observation of the absorber spectrum alone.

Unfortunately, the line widths attained have not been adequate to fully resolve the hyperfine spectra detected. It is

hoped that with the background of these experiments, better sources and absorbers can be made. These should eventually make it possible to study the very interesting magnetic properties of the rare earth metals at low temperatures.

References

1. R. L. Mössbauer, Naturwissenschaften 45, 538 (1958); Z. Naturforsch 14a, 211 (1959); Z. Physik 151, 125 (1959).

2. R. L. Mössbauer, F. W. Stanek, W. H. Wiedemann, Z. Physik 161, 388 (1961).

3. S. Ofer, P. Avivi, R. Bauminger, J. Marinov, S. G. Cohen, Phys. Rev. 120, 406 (1960).
R. Bauminger, S. G. Cohen, A. Marinov, S. Ofer, Phys. Rev. Letters 6, 467 (1961).

4. M. Kalvius, P. Kienle, K. Bochmann, H. Eicher, Z. Physik 163, 87 (1961).

5. R. V. Pound, G. A. Rebka, Jr., Phys. Rev. Letters 4, 274 (1960).

6. S. DeBenedetti, G. Lang, R. Ingalls, Phys. Rev. Letters 6, 60 (1961).

7. F. H. Spedding and A. H. Daane (Ed.), The Rare Earths, 1961, New York.

8. J. B. Gruber, J. G. Conway, J. Chem. Phys. 32, 1531 (1960); J. Chem. Phys. 32, 1178 (1960).

9. W. Low, Paramagnetic Resonance in Solids, 1960, New York.

10. R. M. Sternheimer, H. M. Foley, Phys. Rev. 102, 731 (1956).

10a. T. Hellivell, Priv. Comm.

11. A. Abragam, Nuclear Magnetism, 1961, London.
H. Kopferman, Nuclear Moments, 1958, New York.

12. S. G. Nilsson, Mat. Fys. Medd. Dan. Vid. Selsk. 29, No. 16 (1955).

13. B. R. Mottelson, S. G. Nilsson, Mat. Fys. Skr. Dan. Vid. Selsk. 1, No. 8 (1959).

14. E. N. Hatch, F. Boehm, P. Marmier, J. W. M. DuMond, Phys. Rev. 104, 745 (1956).

15. B. R. Judd, I. Lindgren, Phys. Rev. 122, 1802 (1961).

16. A. Y. Cabezas, I. Lindgren, Phys. Rev. 120, 920 (1960).

17. K. Runge, E. Hatch, Priv. Comm.

18. A. H. Cooke, D. T. Edmonds, F. R. McKim, W. P. Wolf, Proc. Roy. Soc. (London) 242A, 246 (1959).